

PAPER • OPEN ACCESS

An overview of magneto-inertial fusion on the Z machine at Sandia National Laboratories














To cite this article: D.A. Yager-Elorriaga *et al* 2022 *Nucl. Fusion* **62** 042015

View the [article online](#) for updates and enhancements.

You may also like

- [AN ULTRA-FAINT GALAXY CANDIDATE DISCOVERED IN EARLY DATA FROM THE MAGELLANIC SATELLITES SURVEY](#)
A. Drlica-Wagner, K. Bechtol, S. Allam et al.
- [Measuring implosion velocities in experiments and simulations of laser-driven cylindrical implosions on the OMEGA laser](#)
E C Hansen, D H Barnak, R Betti et al.
- [Fusion-neutron measurements for magnetized liner inertial fusion experiments on the Z accelerator](#)
K D Hahn, G A Chandler, C L Ruiz et al.

An overview of magneto-inertial fusion on the Z machine at Sandia National Laboratories

D.A. Yager-Elorriaga* , M.R. Gomez , D.E. Ruiz , S.A. Slutz, A.J. Harvey-Thompson, C.A. Jennings, P.F. Knapp, P.F. Schmit , M.R. Weis , T.J. Awe, G.A. Chandler, M. Mangan, C.E. Myers , J.R. Fein , B.R. Galloway , M. Geissel , M.E. Glinsky , S.B. Hansen , E.C. Harding, D.C. Lamppa, W.E. Lewis , P.K. Rambo, G.K. Robertson, M.E. Savage, G.A. Shipley , I.C. Smith, J. Schwarz, D.J. Ampleford , K. Beckwith, K.J. Peterson , J.L. Porter, G.A. Rochau and D.B. Sinars 

Sandia National Laboratories, Albuquerque, NM 87185, United States of America

E-mail: dayager@sandia.gov

Received 9 June 2021, revised 31 August 2021

Accepted for publication 7 October 2021

Published 7 February 2022



CrossMark

Abstract

We present an overview of the magneto-inertial fusion (MIF) concept Magnetized Liner Inertial Fusion (MagLIF) pursued at Sandia National Laboratories and review some of the most prominent results since the initial experiments in 2013. In MagLIF, a centimeter-scale beryllium tube or ‘liner’ is filled with a fusion fuel, axially pre-magnetized, laser pre-heated, and finally imploded using up to 20 MA from the Z machine. All of these elements are necessary to generate a thermonuclear plasma: laser preheating raises the initial temperature of the fuel, the electrical current implodes the liner and quasi-adiabatically compresses the fuel via the Lorentz force, and the axial magnetic field limits thermal conduction from the hot plasma to the cold liner walls during the implosion. MagLIF is the first MIF concept to demonstrate fusion relevant temperatures, significant fusion production ($>10^{13}$ primary DD neutron yield), and magnetic trapping of charged fusion particles. On a 60 MA next-generation pulsed-power machine, two-dimensional simulations suggest that MagLIF has the potential to generate multi-MJ yields with significant self-heating, a long-term goal of the US Stockpile Stewardship Program. At currents exceeding 65 MA, the high gains required for fusion energy could be achievable.

Keywords: magneto inertial fusion, inertial confinement fusion, Z-machine, magnetized target fusion, Z-pinch, MagLIF, magnetized liner inertial fusion

(Some figures may appear in colour only in the online journal)

* Author to whom any correspondence should be addressed.



Original content from this work may be used under the terms of the [Creative Commons Attribution 4.0 licence](https://creativecommons.org/licenses/by/4.0/). Any further distribution of this work must maintain attribution to the author(s) and the title of the work, journal citation and DOI.

1. Introduction

Inertial confinement fusion (ICF) aims to assemble and confine a dense, high pressure fusion fuel over a relatively short timescale ($\ll 1 \mu\text{s}$) compared to magnetic confinement fusion ($> 1 \text{ s}$). This is typically accomplished by imploding a spherical capsule containing fusion fuel at high implosion velocities ($> 350 \text{ km s}^{-1}$) to obtain the fuel temperatures ($> 4 \text{ keV}$) and areal densities ($\rho R > 0.3 \text{ g cm}^{-2}$) required for ignition [1–4]. Magneto-inertial fusion (MIF) [5–10] utilizes magnetic fields that relax these requirements by limiting thermal conduction losses and introducing magnetic confinement of charged fusion products. On the Z machine at Sandia National Laboratories [11–13], we are pursuing a specific pulsed-power [14] driven MIF concept called Magnetized Liner Inertial Fusion (MagLIF) [15–17]. MagLIF is the first MIF concept to demonstrate fusion-relevant temperatures, significant neutron production and magnetic trapping of charged fusion products [18–22]. Furthermore, numerical simulations show MagLIF has the potential to scale to multi-MJ yields and generate significant fuel self-heating on a next-generation pulsed power machine [23, 24].

In MagLIF, a centimeter-scale cylindrical tube, or ‘liner’, is filled with fusion fuel (deuterium gas on Z experiments) and axially pre-magnetized to 10–20 T using Helmholtz-like coils. The fuel is then pre-heated to an average temperature of 100s of eV via inverse Bremsstrahlung absorption of 527 nm photons from a kilojoule-class laser. Finally, the liner is radially imploded over $\sim 100 \text{ ns}$ via the Lorentz force to velocities of $\sim 70 \text{ km s}^{-1}$ using up to 20 MA of current from the Z machine. This process is schematically demonstrated in figure 1. The laser preheat increases the initial adiabat of the fuel, which is then compressed in a quasi-adiabatic implosion to reach fusion-relevant conditions. The axial magnetic field, which flux-compresses to $> 1000 \text{ T}$ near peak convergence, limits thermal conduction losses from the hot fusion fuel to the comparatively cold liner walls during the implosion and furthermore increases trapping of charged fusion particles in the radial direction at stagnation.

The first MagLIF experiments were conducted in 2013 and demonstrated that the axial magnetic field, the laser preheat, and the implosion are all required to generate thermonuclear fusion yields [18]. Without any one of these inputs, no significant yield could be generated. Utilizing pure deuterium fuel, these experiments produced fuel temperatures of 2.5 keV, neutron energy spectra consistent with a thermonuclear plasma, and produced yields up to 2×10^{12} neutrons. This yield and temperature correspond to a ‘DT-equivalent’ energy of 0.3 kJ, which is the energy that would have been produced if the fuel were initially an equimolar mixture of DT gas. This energy is calculated by (1) determining the number of DT fusion reactions that would have occurred based on the measured DD neutron yield and ratio of DT-to-DD fusion reactivities (assuming an ion temperature equal to the measured value) and (2) multiplying this number by the DT-fusion energy released per reaction, 17.6 MeV. Analysis of the secondary neutron spectra and yield (i.e. neutrons generated from DD-produced tritons fusing with deuterium) demonstrated that the fuel column was highly

magnetized, with the fuel radius exceeding the average Larmor radius of fast tritons, a promising and necessary requirement for trapping of alpha particles [20, 21]. The input conditions of these MagLIF experiments included an axial magnetic field of $B_z = 10 \text{ T}$, peak current of $I_{\text{max}} = 18 \text{ MA}$, and a preheat energy coupled to the fuel of $E_{\text{preheat}} = 0.5 \text{ kJ}$. Over the last decade, experiments have increased the performance of the MagLIF platform by simultaneously increasing the axial magnetic field to 16 T, the laser preheat to 1.2 kJ and the current coupling to 20 MA. Presently, the highest performing MagLIF experiments have achieved burn-averaged ion temperatures of 3.1 keV and primary DD yields of 1.1×10^{13} (a DT-equivalent energy of 2 kJ) [25].

The MagLIF concept is not limited to magnetically driven liners. Fully integrated, laser-driven MagLIF is being explored at the OMEGA facility at the Laboratory for Laser Energetics. These experiments are conducted with scaled-down targets relative to Z experiments and provide the first insight into how MagLIF performance scales as a function of energy delivered to the liner [26–31].

This manuscript presents an overview of MagLIF research at Sandia National Laboratories. In section 2, we discuss the key physics governing a MagLIF system. In section 3, we review the experimental implementation and generation of thermonuclear conditions in MagLIF. In section 4, we discuss major ongoing research areas in MagLIF including implosion stability, material mixing, laser preheat energy coupling, current delivery, and axial magnetic field generation. In section 5, we discuss the scaling of MagLIF to high yields and high gains. Finally, in section 6 we comment on the suitability of MagLIF as an energy producing system.

2. A simple model for MagLIF

In the following sections, we present a simple model that describes the major physical processes that occur in a MagLIF experiment, including the liner implosion and fuel energetics.

2.1. Liner dynamics

A MagLIF implosion can be modeled as a thin, cylindrical metal shell which is magnetically-driven to compress fusion fuel in its interior. The acceleration of such a ‘thin-shell’ is determined by

$$\hat{m} \frac{d^2 R}{dt^2} = -2\pi R (p_{\text{out}} - p_{\text{in}}). \quad (1)$$

Here $R(t)$ is the radius of the shell, p_{out} and p_{in} are the pressures on the outer and inner liner surfaces (defined below), and \hat{m} is the liner mass per-unit-length defined as

$$\hat{m} = \pi \rho_{\text{liner},0} (R_{\text{out},0}^2 - R_{\text{in},0}^2), \quad (2)$$

where $\rho_{\text{liner},0}$ is the initial mass density of the actual finite-thickness liner, $R_{\text{out},0} = R_0$ is the initial liner outer radius, and $R_{\text{in},0}$ is the initial liner inner radius. For thin shells, it is customary to introduce the liner aspect ratio $\text{AR} = R_{\text{out},0}/\delta R_0 \gg 1$, where $\delta R_0 = R_{\text{out},0} - R_{\text{in},0}$ is the initial liner width. In terms

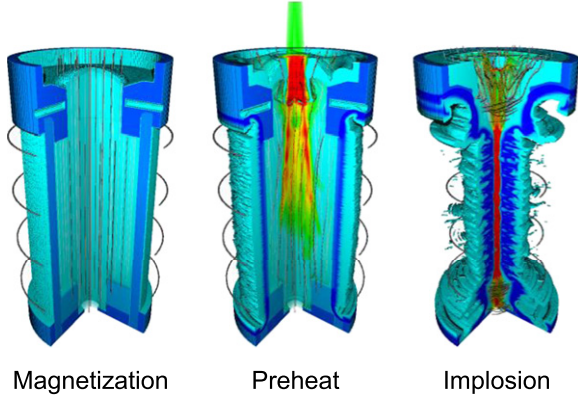


Figure 1. Three-dimensional simulation demonstrating the three stages of MagLIF. Reprinted figure with permission from Gomez *et al* 2014 *Phys. Rev. Lett.* **113** 155004. Copyright 2014 by the American Physical Society <https://doi.org/10.1103/PhysRevLett.113.155003>.

of AR, the liner mass per-unit-length is approximately $\hat{m} \simeq 2\pi\rho_{\text{liner},0}R_0^2/\text{AR}$.

The trajectory of the liner radius in equation (1) is dictated by the outer and inner pressure sources. In MagLIF, $p_{\text{out}}(t)$ is given by the magnetic pressure exerted on the liner outer surface, calculated using Ampère's law:

$$p_{\text{out}} = \frac{B_\theta^2}{2\mu_0} = \frac{\mu_0 I^2}{8\pi^2 R^2}, \quad (3)$$

where $B_\theta(t)$ is the azimuthal magnetic field, $I(t)$ is the electrical current flowing along the liner's outer surface, and μ_0 is the magnetic permeability.

In equation (1), $p_{\text{in}}(t)$ denotes the internal pressure exerted by the compressed fusion fuel (the internal magnetic pressure due to the axial magnetic field is neglected in this model). We treat the fuel as an ideal gas so that the fuel pressure can be written in the following equivalent manner:

$$p_{\text{in}} = \frac{2\rho k_B T}{m_i} = \frac{2}{3} \frac{\hat{U}}{\pi R^2}. \quad (4)$$

Here ρ is the fuel mass density, T is the fuel temperature and \hat{U} is the internal energy of the fuel per-unit-length (from here forward, all 'hat' quantities denote per-unit-length). Also, k_B is the Boltzmann constant, $m_i = Am_p$ is the ion mass where A is the average atomic number for the fusion fuel ($A = 2.5$ for equimolar DT plasma) and m_p is the proton mass. In equation (4), the factor 2 takes into account the electron contribution to the total fuel pressure, where we assumed that the plasma is completely ionized ($Z = 1$) and that the electrons and ions have the same temperature.

2.2. Fuel energetics

The fuel energetics may be described by a simple model capturing the fuel internal energy. The equation for \hat{U} is given by

$$\frac{d\hat{U}}{dt} = \hat{P}_{\text{preheat}} + \hat{P}_{\text{PdV}} + \hat{P}_\alpha - \hat{P}_{\text{rad}} - \hat{P}_c - \hat{P}_{\text{end}}. \quad (5)$$

Here \hat{P}_{preheat} is the preheating rate, \hat{P}_{PdV} is the adiabatic heating rate, \hat{P}_α is the heating rate due to DT fusion α -particle energy deposition, \hat{P}_{rad} is the radiative cooling rate, \hat{P}_c is the cooling rate due to conduction losses, and \hat{P}_{end} is the cooling rate due to mass outflows through the ends of the open cylindrical liner.

In the case of MagLIF prior to preheat, the internal gas pressure is negligible compared to the compressive pressure of the pulsed-power driver [$\mathcal{O}(\text{bar})$] vs [$\mathcal{O}(\text{Mbar})$]. Therefore, before the time of preheat, it is a good approximation to entirely neglect the fuel internal energy. For this simple model, we may assume that the preheat energy is instantaneously deposited uniformly into the fuel (in reality, preheat energy is delivered in a ~ 5 ns window compared to the ~ 100 ns duration of the implosion). Thus, in this approximation, the fuel preheating rate is

$$\hat{P}_{\text{preheat}} = \hat{E}_{\text{preheat}} \delta(t - t_{\text{preheat}}), \quad (6)$$

where t_{preheat} is the time at which preheat occurs and \hat{E}_{preheat} is the preheat energy deposited into the fuel.

After preheat, the imploding liner performs work on the fuel in its interior. The PdV heating rate is given by

$$\hat{P}_{\text{PdV}} = -p_{\text{in}}(t) \frac{d}{dt} \pi R^2 = -\frac{4\rho k_B T}{m_i} \pi R \dot{R} = -\frac{4}{3} \hat{U} \frac{\dot{R}}{R}, \quad (7)$$

where we have substituted equation (4).

We assume that the dominant mechanism for radiation losses is electron Bremsstrahlung emission. We also assume that the fuel plasma is optically thin and that any radiation energy deposited into the liner does not alter the implosion dynamics. Therefore, the approximate energy loss rate from a hot, uniform, cylindrical hydrogen plasma is [32]

$$\hat{P}_{\text{rad}} = \frac{64}{3\sqrt{2\pi}} \left(\frac{e^2}{4\pi\epsilon_0} \right)^3 \frac{1}{m_e c^2 \hbar} \sqrt{\frac{k_B T}{m_e c^2}} \frac{Z^3 \rho^2}{m_i^2} \pi R^2, \quad (8)$$

where e is the elementary charge, ϵ_0 is the permittivity of free space, m_e is the electron mass, $\hbar = h/(2\pi)$ is the reduced Planck constant, and c is the speed of light. The last factor πR^2 corresponds to the cross-sectional area of the plasma cylinder. Note that there are other sources of radiation losses, for example, from mix of the liner material into the fuel, which we do not consider here.

Thermal conduction is another mechanism from which the plasma can lose energy. Due to the radial compression of MagLIF, thermal conduction losses are dominated by thermal flux in the radial direction. Therefore, the energy loss rate due to electron and ion conduction is approximately given by

$$\hat{P}_c = 2\pi R(\kappa_{ce} + \kappa_{ci}) \partial_r(k_B T) \simeq 2\pi(\kappa_{ce} + \kappa_{ci}) k_B T, \quad (9)$$

where $\partial_r T \simeq T/R$. Here κ_{ce} and κ_{ci} correspond to the electron and ion thermal conductivities, respectively. Due to the relatively slow compression rate of MagLIF compared to its laser ICF counterparts, the cylindrical plasma must be axially magnetized in order to prevent excessive heat conduction losses. For $Z = 1$, the electron and ion thermal conductivities for a magnetized plasma are respectively given by [33]

$$\kappa_{ce} = \frac{\rho}{m_i} \frac{k_B T}{m_e} \tau_{\text{e}} \text{ge}(x_e), \quad (10)$$

$$\kappa_{ci} = \frac{\rho}{m_i} \frac{k_B T}{Am_p} \tau_i g_i(x_i), \quad (11)$$

where τ_e and τ_i are the electron–ion and ion–ion collision times:

$$\tau_e = \frac{3(4\pi\epsilon_0)^2 m_i \sqrt{m_e} (k_B T)^{3/2}}{4\sqrt{2}\pi Z^2 \rho e^4 \ln \Lambda}, \quad (12)$$

$$\tau_i = \frac{3(4\pi\epsilon_0)^2 m_i^{3/2} (k_B T)^{3/2}}{4\sqrt{\pi} Z^4 \rho e^4 \ln \Lambda}. \quad (13)$$

In equations (10)–(13), $\ln \Lambda$ is the Coulomb logarithm and the functions g_e and g_i describe the dependence of the thermal conductivities on the axial magnetic field. The latter are given by

$$g_e(x) = \frac{11.92 + 4.664x^2}{3.7703 + 14.79x^2 + x^4}, \quad (14)$$

$$g_i(x) = \frac{2.645 + 2x^2}{0.677 + 2.7x^2 + x^4}. \quad (15)$$

Finally, $x_e = \Omega_e \tau_e$ and $x_i = \Omega_i \tau_i$ are the electron and ion Hall parameters and $\Omega_e = eB/m_e$ and $\Omega_i = ZeB/m_i$ are the electron and ion gyrofrequencies.

In MagLIF, there are openings at the top and bottom of the target to inject fuel and preheat energy. Once the implosion is underway, hot fuel can leave the liner interior through these openings and take energy along with it. These end losses limit the efficacy of adiabatic heating and reduce the total number of deuterons and tritons in the fuel. A semi-analytic treatment of end losses can be found in reference [34]. Numerical simulations indicate that, depending on the preheat energy, up to 50% of the initial mass can escape axially during the implosion [15, 17].

Summarizing this system, we see that the current delivered to the liner determines the magnetic pressure driving the liner, which quasi-adiabatically compresses the fuel. The initial temperature of the fuel is increased via laser preheating and is required to allow the system to reach thermonuclear conditions. Compression is not perfectly adiabatic due to a combination of radiation losses, thermal conduction losses, and end losses. The axial magnetic field, which can be compressed to >1000 T at stagnation, limits thermal conduction losses from the fuel to the cold liner wall during the ~ 50 ns implosion time between preheat and stagnation.

With sufficient preheat and current drive, \hat{P}_α can become a dominant energy source in a DT fuel, bootstrapping the fuel to even higher energies and making large gains possible. This process is enhanced by the axial magnetic field, which impedes charged fusion particles propagating in the radial direction, allowing them to deposit a larger fraction of their energy before escaping. To quantify alpha trapping, a parameter often used is the magnetic field-radius product, BR , which characterizes the ratio of the radius of the stagnated fuel column to the Larmor radius of the thermonuclear alpha particles. Figure 2 demonstrates the effect of increasing BR using a Lindl diagram [1], where contours with $dT/dt = 0$ are plotted as a function of fuel temperature and areal density [21]. In this diagram,

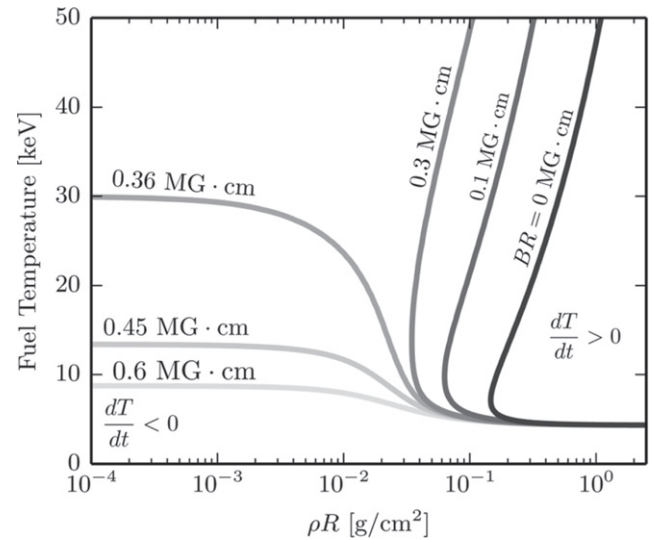


Figure 2. Lindl diagram [1] demonstrating self-heating requirements as a function of fuel temperature and areal density. The magnetization BR relaxes the areal density requirements and opens a wide area of parameter space for self-heating. Reproduced from Knapp et al 2015 *Phys. Plasmas* 22 056312 with the permission of AIP Publishing <https://doi.org/10.1063/1.4920948>.

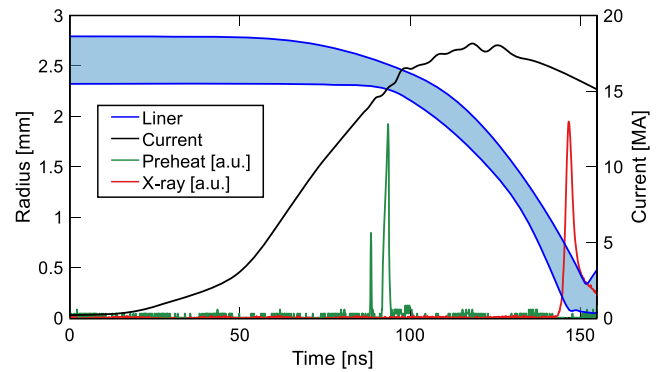


Figure 3. Semi-analytic calculation capturing the evolution of a MagLIF target. The current delivered to the target in the calculation (black), liner trajectory (blue), experimental laser preheat monitor signal (green) and experimental x-ray signal (red) are plotted. Laser preheat begins to heat the target just as the inner surface of the liner begins to implode.

regions with $dT/dt > 0$ (generally toward the upper right of the contours) will self-heat. As BR increases, areal density becomes significantly less important and opens the parameter space for achieving self-heating. For reference, present-day MagLIF experiments have already demonstrated relevant magnetization levels at ~ 0.2 – 0.45 MG cm [35].

It is worth noting that the model described above is a simplified model incorporating the dominant mechanisms in a MagLIF system. A semi-analytic model was developed to better account for the physics of MagLIF by including (1) fuel preheat via laser absorption; (2) coupling of the electrical current via an electrical circuit; (3) liner dynamics via finite thickness and compressibility; and (4) magnetic field dynamics including Nernst effects [34, 36]. In figure 3, we show a

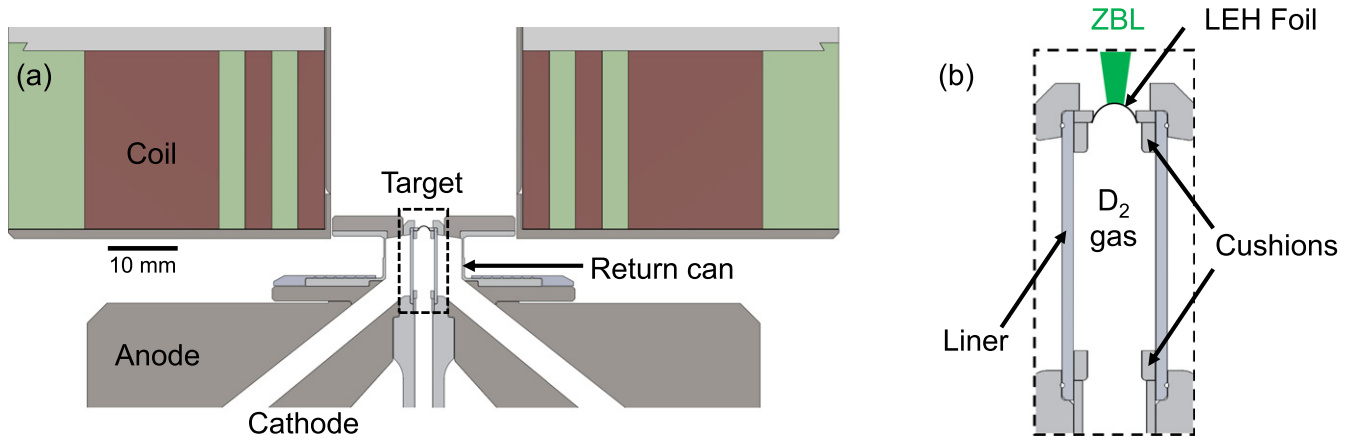


Figure 4. Cross sections of a typical (a) load hardware configuration and (b) MagLIF target, including the ZBL preheat path.

calculation using this semi-analytic model of a MagLIF system driven with 18 MA from the Z machine. The calculation shows that the inner boundary of the liner begins to implode at roughly 14 MA, at which point the laser preheat process is initiated. The liner continues to implode for approximately 55 ns, during which the fuel is quasi-adiabatically compressed to fusion conditions, culminating in a ns-scale burst of x-rays and neutrons.

A more complete description of MagLIF must additionally account for the development of Rayleigh–Taylor-like instabilities in the liner which can degrade fuel compression, reduce the inertial confinement, increase the residual kinetic energy of the stagnated fuel, and introduce liner-fuel mixing. The physics of laser preheat energy deposition into the fuel prior to compression is also essential. This includes laser absorption and backscatter due to a thin polyimide window containing the fuel, laser self-focusing and filamentation, and laser absorption of the fuel itself. Finally, the power flow coupling of electrical energy to magnetic energy delivered to the liner is important. The physics of these systems are active areas of research in the field and will be reviewed in section 4. A comprehensive understanding of them, along with their scaling to larger machines, will be critical for determining the viability of MagLIF as a high yield and energy producing system.

3. Demonstration of thermonuclear fusion in MagLIF

The first MagLIF experiments were conducted in 2013 and established MagLIF as the first MIF concept to demonstrate fusion-relevant temperatures, significant neutron production ($>10^{12}$ DD-produced neutrons), and magnetic trapping of charged fusion products [18, 20–22]. These experiments also demonstrated that a simultaneous application of current, laser preheat, and axial magnetic field to the target was essential to produce significant fusion yields. Experiments with no axial magnetic field and no laser preheating produced a factor of ~ 1000 fewer neutrons compared to fully integrated experiments (where integrated experiments incorporate the pre-imposed axial magnetic field, laser preheat, and magnetically

driven implosion). Subsequent experiments with no laser preheat (but with an axial magnetic field) and with no axial magnetic field (but with laser preheat) produced ~ 200 and ~ 50 fewer neutrons, respectively. The importance of including the axial magnetic field and fuel preheat is discussed in reference [15].

Cross sections of typical MagLIF load hardware and targets are shown in figure 4. The target consists of a beryllium liner characterized by its outer radius and aspect ratio, the latter of which is an indicator of the robustness of the target to instability feedthrough from the outer to inner radius, with lower AR targets generally exhibiting improved stability. MagLIF targets have been fielded with AR 4.6, 6 and 9, with AR6 being the most common option. 2D simulations show performance degrades compared to 1D calculations due to instability development for aspect ratios above $AR \gtrsim 6$ and indicate an optimum in performance near this value [15]. AR9 targets are often coated with $70 \mu\text{m}$ of dielectric to improve stability (see section 4.1). Most targets fielded to date utilize an inner radius of $R_{\text{in},0} = 2.325 \text{ mm}$. The imploding height is typically 10 mm and determined by the distance between a pair of beryllium cushions inside of the liner. The cushions prevent the growth of a wall instability that would otherwise cause these regions of the target to prematurely implode and possibly inject contaminants into the fuel [37, 38]. The liner is filled from the bottom with DD fuel at $0.7\text{--}1.4 \text{ mg cm}^{-3}$ and sealed using a thin polyimide foil 0.47 to $3.5 \mu\text{m}$ thick on the top of the target. This thin foil is referred to as the laser entrance hole (LEH) window. The target is magnetized to $10\text{--}20 \text{ T}$ using Helmholtz-like coils driven by an external capacitor bank several ms prior to the Z discharge to allow the field to uniformly diffuse through the conductive hardware and target while preventing a buckling instability in the target itself [39]. Note the coil configuration shown in figure 4(a) utilizes a single coil above the target, introducing a 30% variation in the axial magnetic field along the axis of the target. Resistive magnetohydrodynamics simulations suggest this non-uniformity does not affect the target dynamics or performance.

The initial experiments coupled 18 MA with a 100 ns risetime to 7.5 mm tall liners via an extended transmission line. Subsequent improvements to the transmission line have

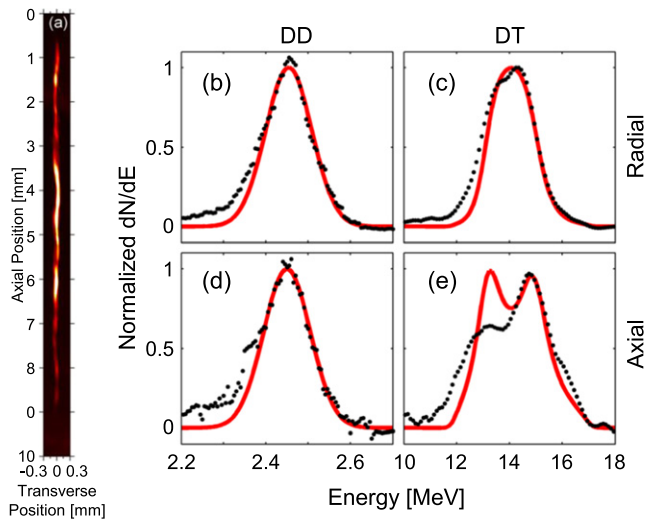


Figure 5. (a) X-ray self-emission image of a thermonuclear stagnation column. (b)–(e) Experimental axial and radial primary DD and secondary DT neutron spectra (black). The leading ends of the primary DD spectra are fit from 2.4 to 2.7 MeV using a temperature of 2.4 keV (red). The DT spectra are similarly fit from 14.1 to 18 MeV using a magnetization $BR = 0.34$ MG cm. Note the leading ends are fit as they are less impacted by neutron scattering. Reproduced from Gomez *et al* 2015 *Phys. Plasmas*. **22** 056306 with the permission of AIP Publishing <https://doi.org/10.1063/1.4919394>.

enabled peak currents of 20 MA with taller (10 mm), more inductive targets. As soon as the inner surface of the liner begins to implode, a 1–4 kJ, 527 nm pulse from the Z-beamlet laser (ZBL) is incident upon the polyimide foil containing the fuel. ZBL is a TW-class, frequency doubled Nd:glass laser [40]. A laser pre-pulse is used to ionize and expand the window and is required to allow sufficient coupling of laser energy to the fuel [41]. Some energy is lost to ablation and backscatter from the foil, ultimately allowing 0.5–1.4 kJ of energy to be coupled to the fuel [42]. The inner surface of the liner subsequently implodes over ~ 55 ns, quasi-adiabatically compressing the fuel to generate a highly converged stagnation column at thermonuclear conditions. MagLIF target designs are typically limited to convergence ratios of $CR < 40$, where $CR = R_{in,0}/R_{in,stag}$ and $R_{in,0}$ and $R_{in,stag}$ are the initial inner and stagnation radii, respectively. Larger convergence ratios increase the risk of disruption in the liner due to instabilities. Experimentally measured values for the convergence ratio based on x-ray self-emission imaging range from a CR of 30 to 40.

An x-ray self-emission image of the fuel column at stagnation is shown in figure 5. The column shows a highly converged region emitting with a weakly helical instability structure, likely arising from helical instabilities that form in the liner during the implosion [38, 43]. Detailed analysis of these structures has recently been performed using the Mallat scattering transformation in order to quantify various morphological features [44]. Neutron spectra obtained using a neutron time-of-flight (NToF) diagnostic [45] are shown in figures 5(b)–(e). The DD spectra were fit using the high-energy regions, which are less affected by scattering, and show a temperature of

2.4 keV. The NToF spectra also show a 14 MeV DT peak, which is anisotropic in the axial and radial directions [20, 21]. The shape of the spectrum contains information on the magnetization and has been used to infer fuel BR values of 0.2–0.45 MG cm [20, 21]. The magnetization of tritons is a reasonable surrogate for alpha particle magnetization due to nearly equal initial gyroradii; therefore, the experimentally inferred BR values indicate MagLIF has already demonstrated significant fuel magnetizations (see figure 2). Indium and copper activation samples show a yield of 2×10^{12} DD (primary) and 5×10^{10} DT (secondary) neutrons. The primary neutron yield and ion temperature indicate a DT-equivalent yield of 0.3 kJ. Time integrated x-ray spectra show an electron temperature of 2.4 keV, consistent with NToF ion temperatures. Electron temperatures are obtained by fitting the high-energy continuum slope, generally from ~ 9 –12 keV, with uncertainties in the 10%–20% range due to variations in the slope. Based on x-ray diodes, the x-ray pulse at stagnation has a 2 ns FWHM, indicating a similar integration time for the spectrometers [18, 22]. Additional x-ray and neutron diagnostics implemented for MagLIF can be found in references [22, 46–51].

Some of the early Z pinch experiments in the 1950s showed neutron production that was attributed to beam–target interactions (and not thermonuclear production), driven by voltages produced by MHD sausage instabilities [52]. With this historical viewpoint in mind, significant effort has gone toward demonstrating that neutrons produced in MagLIF are of thermonuclear origin—a critical requirement for any ICF concept that hopes to scale to ignition. Evidence supporting the thermonuclear nature of the neutrons include a number of observations. First, significant yield is only measured when the fusion fuel is preheated and magnetized, indicating that the fuel requires an initial, sufficiently hot temperature that is not cooled by thermal conduction to the cold liner walls. Beam–target produced neutrons from deuterons accelerated by high voltages should largely be ambivalent to the temperature but rather scale as a function of density of the deuterium fuel. Similarly, fusion yields are significantly reduced when radiation losses are intentionally enhanced via the introduction of high Z dopants to the fusion fuel. Second, the primary (DD) neutron yields and spectra are found to be isotropic, whereas beam–target interactions are expected to preferentially produce neutrons along strong electric field lines. Third, the measured and inferred fuel parameters at stagnation are consistent with simulated values assuming thermonuclear fusion production. Finally, close examination of an ensemble of MagLIF experiments shows the expected scaling of primary DD neutron yield with ion temperature consistent with the DD fusion reactivity. This plot is shown in figure 6 and also captures improvements to the MagLIF platform since the early experiments. Additional studies assessing stagnation conditions and identifying trends may be found in reference [53].

4. Major research areas in MagLIF

4.1. Instability development

Traditional ICF targets are susceptible to the Rayleigh–Taylor (RT) instability [54, 55], which arises when a light fluid

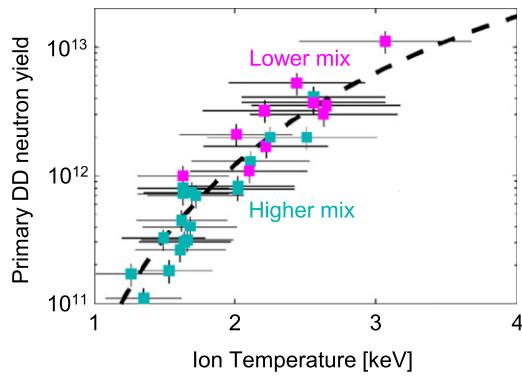


Figure 6. Primary DD neutron yield as a function of ion temperature. The yield is separated into higher (teal) and lower (magenta) mix targets. The fusion reactivity for DD- ^3He fusion [34], scaled by 3.9×10^{38} , is plotted (dashed line) showing performance is consistent with thermonuclear fusion production. Reprinted figure with permission from Gomez *et al* 2020 *Phys. Rev. Lett.* **125** 155002. Copyright 2020 by the American Physical Society <https://doi.org/10.1103/PhysRevLett.125.155002>.

accelerates a heavy fluid. This occurs in the outer boundary of an imploding spherical capsule and in the inner boundary during the deceleration of the capsule onto a high-pressure fuel. In experiments leading up to integrated MagLIF, a major concern was whether the magneto Rayleigh–Taylor (MRT) [56–61] instability would preclude a sufficiently stable liner to assemble and inertially confine a thermonuclear fusion fuel. MRT arises when the magnetic field (which acts as the light fluid) accelerates the beryllium liner (heavy fluid) and, similar to traditional ICF, when the ‘heavy’ liner decelerates onto the ‘light’ magnetized fusion fuel.

To ensure our modeling tools could capture the physics of MRT, we first conducted controlled radiographic experiments with imploding liners that were pre-seeded with machined sinusoidal perturbations [62, 63]. With a known seed, we could track the perturbation growth as it evolved to factors of ~ 50 of its original amplitude. Encouragingly, the pre-shot simulations reproduced the experimental data, including key features such as the formation of ablated jets in the bubble region between the larger radii ‘spikes’. A comparison of the experimental data to simulations is shown in figure 7.

Subsequent efforts were directed at understanding instability growth in smooth beryllium liners with a root-mean-square surface roughness of 100–250 nm [37, 64]. These experiments demonstrated a higher than expected level of azimuthal correlation, well beyond what 3D MHD models predicted. The models could only reproduce the experimental data when the randomly generated initial surface perturbation was modified to increase the azimuthal correlation of the perturbations at randomly chosen axial locations, as shown in figure 8. More surprisingly, experiments with liners that had been post-processed to remove the azimuthal tooling finish and had been axially polished (leaving axial, rather than azimuthal grooves) demonstrated high levels of azimuthal symmetry, despite a complete lack of azimuthal seed.

Recent work has suggested that the higher-than-expected azimuthal correlation could be related to key missing physics

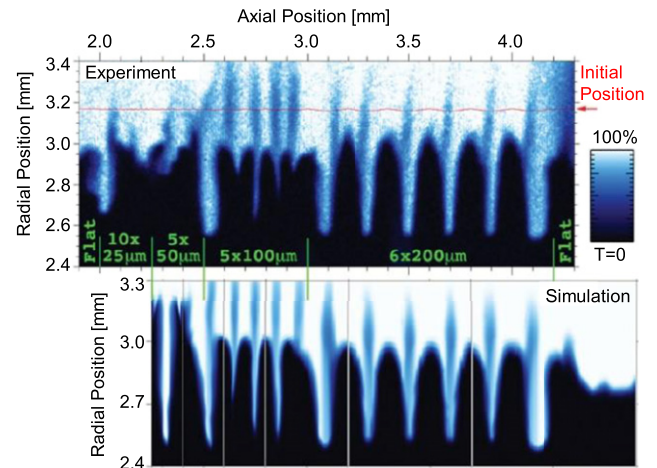


Figure 7. (a) Experimental and (b) simulated radiographs capturing the evolution of the MRT instability in a magnetically driven aluminum liner. The initial seed for the instability is shown in red. Reprinted figure with permission from Sinars *et al* 2010 *Phys. Rev. Lett.* **105** 185001. Copyright 2010 by the American Physical Society <https://doi.org/10.1103/PhysRevLett.105.185001>.

in the seeding of the MRT instability. Presently, it is proposed that the early time electrothermal instability (ETI) [65–75] could explain the azimuthal correlation, even with axially-finished targets. This instability arises due to localized current enhancement in materials where the resistivity increases with temperature and/or decreases with density. A positive perturbation in current (e.g. due to current flowing around resistive inclusions or pits on the surface of the target) increases the Joule heating to this region and therefore its resistivity. As a result, current is concentrated in nearby azimuthal regions, further increasing the resistivity and subsequent ohmic heating. This feedback loop continues to drive localized heating along predominantly azimuthally-oriented bands, which eventually explode and produce density perturbations. This further increases the resistivity, which for ablated metals like Be and Al increases with decreasing density, and provides an azimuthal seed for MRT. The evolution of this instability typically ceases when the resistivity of the material enters a Spitzer-like regime; however, at this point, the MRT instability has been seeded and will continue to dominate perturbation growth in the liner. High resolution simulations were conducted in 2D [66–68] and 3D [76] that demonstrate this process. Experiments were conducted by radiographing electrically pulsed rods on the Z machine and demonstrated excellent agreement with 2D simulations including ETI physics when initialized with the as-machined surface contours [66, 67].

The agreement with experimental data encouraged a solution to mitigate MRT by controlling the ETI seed. Dielectric materials where the resistivity, η , and temperature, T , satisfy $d\eta/dT < 0$ are inherently stable to azimuthally correlated ETI growth. Simulations showed that applying a relatively thick dielectric tamper ($\sim 50 \mu\text{m}$) to the outer surface of a magnetically driven liner significantly reduces the overall MRT growth by limiting the ETI growth in the underlying material via two mechanisms [68]. First, the dielectric acts as a hydrodynamic tamper to limit the ETI-driven explosions of the underlying

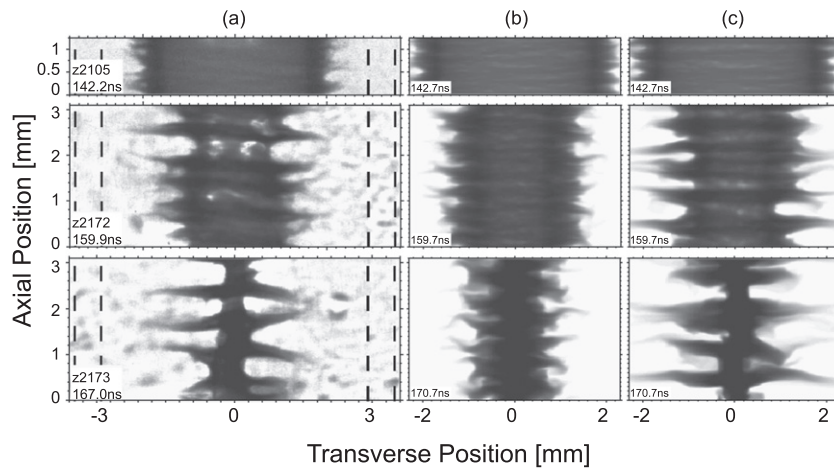


Figure 8. Radiographs of magnetically imploded, empty beryllium liners with no pre-seeded axial magnetic field [64]. The experimental data (a) is compared to 3D Gorgon simulations with (b) random and (c) azimuthally biased initial seeds. The excellent agreement between the data and biased-simulation suggests there is an early time, azimuthally correlating process subsequently attributed to the electrothermal instability. Reprinted figure with permission from McBride *et al* 2012 *Phys. Rev. Lett.* **109** 135004. Copyright 2012 by the American Physical Society <https://doi.org/10.1103/PhysRevLett.109.135004>.

material. Second, by tamping these explosions, the underlying material is kept dense so that the ETI growth rate, which decreases with increasing density, is reduced [65].

Experiments with dielectric coatings applied to rods and liners (in both implosion-only and fully integrated MagLIF experiments) validated these simulations by demonstrating significant improvements to the stability of the targets [68, 77, 78]. Figure 9 compares the instability development of imploding aluminum liners and MagLIF stagnation columns with and without a dielectric coating. Confoundingly, the more stable targets at lower aspect ratios (e.g. AR6) have produced lower yields than their uncoated counterparts. While no satisfactory explanation has been given, a possible scenario is the dielectric does not fully implode with the target and provides a parallel current path that reduces the magnetic pressure on the liner, which in turn could impact assembly and confinement of the fuel. Unfortunately, correctly modeling the dielectric breakdown process with MHD tools is challenging and assumptions, such as the dielectric breakdown threshold, can fundamentally change the dynamics of the dielectric material.

A new instability puzzle arose when adding a pre-seeded axial magnetic field to magnetically imploded liners [38, 43]. In MagLIF, the azimuthal magnetic field generated from the current carried by the liner was expected to greatly exceed the relatively small pre-seeded axial magnetic field. In this situation ($B_\theta \gg B_z$), the growth rate of the MRT instability is maximized for $m = 0$ ‘sausage’ instability modes (m is the azimuthal mode number), as the stabilizing magnetic tension is negligible for perturbations with purely axial modes (e.g. azimuthally symmetric modes) [59–61, 79, 80]. Indeed, implosion-only radiography experiments with no axial magnetic field demonstrate azimuthally correlated instability structures as previously discussed; however, introducing the axial magnetic field modified this instability structure and produced helical instability modes (modes with $m > 0$, see figure 10) that persisted throughout the implosion, increasing in pitch angle despite the rapidly decreasing ratio of *initially* applied

axial to *time-dependent* azimuthal magnetic field. This was contrary to expectation, as the pitch angle of the instability was expected to roughly follow the global magnetic field orientation external to the liner and the axial magnetic field was not expected to dramatically increase (note the ratio of $B_z(t)/B_\theta(t)$ is a challenging measurement that has not been obtained). Interestingly, simulations with artificially seeded helical grooves continued to evolve with predominantly helical instabilities similar to the experiment [43]. This suggests that, once appropriately seeded, helical modes persist and therefore that the missing physics lies in the origin of the helical mode.

A variety of hypotheses have been posed addressing the origin of the helical instability, including: (1) magnetic flux compression by low-density plasmas produced in the transmission line leading up to the target enhances the axial magnetic field and yields a dominantly helical MRT growth rate throughout the implosion [81, 82]; (2) the ETI instability is itself helically modified by the axial magnetic field, providing a helical seed for the subsequent MRT [83]; and (3) low density plasma generated in the transmission line undergoes an upper hybrid oscillation that bombards the surface of the liner with charged particles oriented in a helical fashion early in time, when B_z is comparable to B_θ , seeding helically resistive perturbations that are enhanced by ETI and subsequently MRT [84]. Experiments testing these hypotheses are underway. Interestingly, thin foil-liner implosion experiments [85] at 1 MA pulsed power drivers recreated helical modes with pre-imposed axial magnetic fields [79, 80, 86, 87], demonstrating these modes are ubiquitous across a variety of scales. Whether the same dominant physics applies at both 1 MA and 20 MA scales is yet to be determined.

Self-consistently modeling the helical instability will be important for assessing the stability of MagLIF liners at larger currents. For present-day MagLIF, several outstanding questions remain, including how helical modes affect fuel assembly and inertial confinement compared to azimuthal modes, how helical modes affect the morphology of the stagnation column,

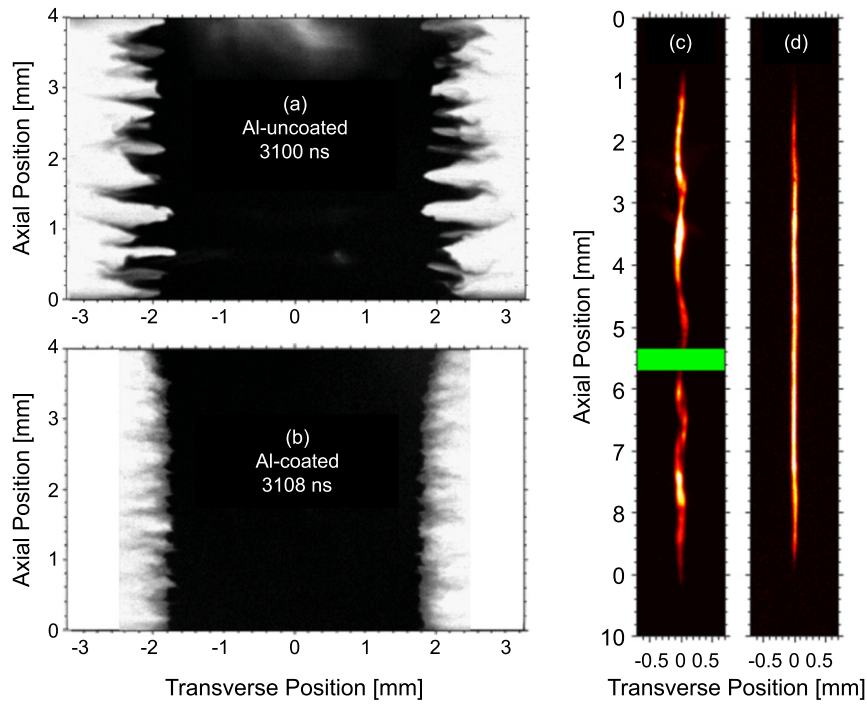


Figure 9. Radiography experiments of (a) uncoated and (b) coated aluminum liners show the in-flight MRT instability is reduced via the application of a dielectric tamper to the outside of the liner. Reprinted figure with permission from Awe *et al* 2016 *Phys. Rev. Lett.* **116** 065001. Copyright 2016 by the American Physical Society <https://doi.org/10.1103/PhysRevLett.116.065001>. Self-emission x-ray images from fully integrated MagLIF experiments with (c) uncoated and (d) dielectric-coated targets (note the green region marks the location of a spatial fiducial) showing enhanced stability of the stagnation column.

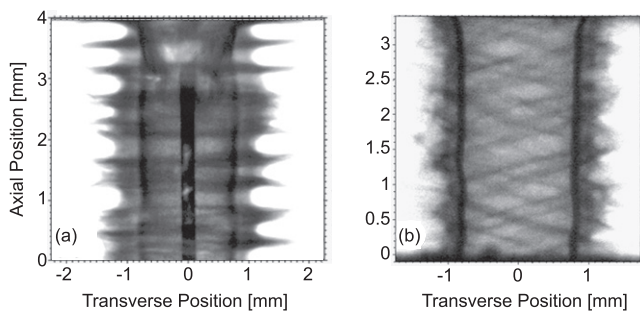


Figure 10. Radiographs of (a) unmagnetized ($B_z = 0$) and (b) magnetized ($B_z = 7$ T) imploding liners, showing sausage ($m = 0$) and helical ($m > 0$) instability development. Reprinted figure with permission from Awe *et al* 2013 *Phys. Rev. Lett.* **111** 235005. Copyright 2013 by the American Physical Society <https://doi.org/10.1103/PhysRevLett.111.235005>.

and how helical modes scale in amplitude and pitch angle with axial magnetic field and applied current.

The above work has focused on the formation and development of MRT. Another related fundamental question concerns the effect of MRT on fuel assembly and confinement. Radiographic experiments enabling direct measurements of the inertial confinement time, τ , and pressure-time product, $P\tau$, demonstrated that areal density variations due to MRT can decrease both the inertial confinement time and attainable fuel pressures [88]. Furthermore, MRT weakens confinement in the bubble regions via mass transport to the spikes, creating regions susceptible to ‘aneurysms’ that can lead to

rapid pressure loss of the fuel [88, 89]. Figure 11 shows radiographic images capturing the development of an aneurysm in a beryllium liner confining a high-pressure deuterium fuel.

We conclude this section with a discussion on our recent efforts to mitigate instabilities, which are categorized into three approaches: (1) mitigating the seed to MRT (e.g. by mitigating ETI); (2) mitigating the MRT instability development on the outside of the liner; and (3) mitigating the MRT feedthrough to the inside of the liner. Addressing the first, experiments on 1 MA pulsed power machines have demonstrated a reduction in ETI-associated emission hotspots on the surface of ultrapure Al rods (99.999% pure) compared to less pure Al 6061 [74], consistent with the notion that ETI originates from localized resistive inclusions in the material. In subsequent experiments with machined pits on the surface of rods, we have observed via self-emission imaging how these perturbations evolve and have benchmarked key features in high resolution 3D MHD simulations [90]. These observations suggest ultrapure target materials and/or coatings that fill in surface pits on Be liners could improve stability by mitigating ETI itself.

To mitigate the MRT instability, a novel dynamic screw pinch (DSP) [91, 92] concept was designed [93] and recently implemented on Z experiments. In a DSP system, a dynamically rotating helical magnetic drive field is generated by modifying the return current structure into discrete, helical posts. As the liner implodes, the self-generated azimuthal magnetic field component increases with respect to the axial field component

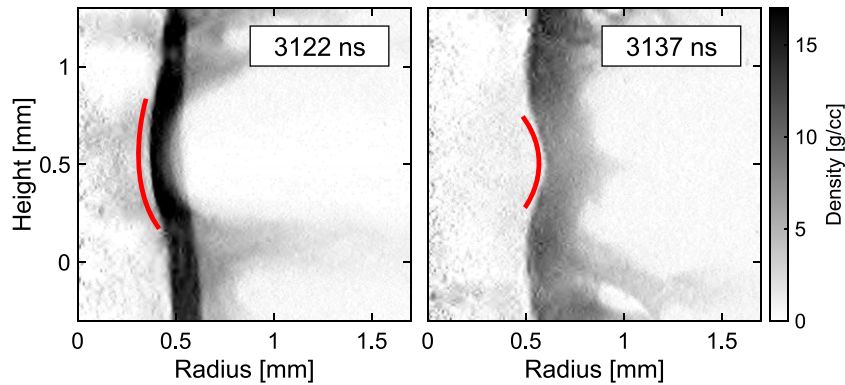


Figure 11. Radiographic images of a magnetically driven liner inertially confining a high-pressure deuterium fuel. As the MRT instability transports mass from the bubble regions to the spikes, the areal density is reduced. The inflection in the bubble shows how these regions can rapidly deform and accordingly decrease the pressure in the fuel. Reproduced from Knapp *et al* 2017 *Phys. Plasmas* **24** 042708 with the permission of AIP Publishing <https://doi.org/10.1063/1.4981206>.

generated by the quasi-solenoidal helical return posts, causing the drive field and associated stabilizing magnetic tension on the surface of the liner to rotate in-flight. When the linear theory is applied to Z relevant targets [91], the total number of instability e-foldings is reduced for a wide variety of azimuthal and axial modes. In particular, the smaller wavelength modes (e.g. modes with wavelength $\lambda \ll 1$ mm) experience a larger reduction in growth. The experimental results on Z are highly encouraging and will be discussed in a future publication.

Finally, mitigating MRT feedthrough is also being explored by fielding thicker (lower AR) targets. To compensate for the increased mass and to not delay the implosion time, the target's initial inner and outer radii are also reduced in order to increase the drive magnetic pressure [94]. Recent experiments have implemented this type of target scaling and have demonstrated improved stagnation column stability along with a shift in the instability spectrum to larger wavelength modes. This is consistent with theoretical analysis of the MRT feedthrough factor [58]. Results from these experiments will be presented in a future publication.

4.2. Mixing of contaminants into the fuel

There are a variety of possible sources of mix in a MagLIF system that can contaminate the fuel and exacerbate radiation losses. The dominant sources include interactions of the pre-heat laser with the polyimide LEH window (discussed in the next section) and the beryllium cushions, interactions of the blast-wave resulting from the preheat laser with the beryllium liner and cushions, radiation ablation of the inner liner wall after preheat, and deceleration-induced mix from the beryllium liner itself. The ultimate effect of mix on performance is a combination of the atomic number and total quantity of the contaminants, and when and where the contaminants are introduced into the fuel. Contaminants introduced during the laser-preheat stage have a significantly longer time to radiate (albeit at initially lower temperatures) than those introduced at stagnation (e.g. deceleration mix), and those that migrate toward the hotter regions of the fuel have a larger impact on the energetics of the fuel than mixing in the cooler fuel regions

near the liner. A detailed sensitivity study of MagLIF to mix may be found in reference [95].

Some of the early MagLIF targets utilized aluminum cushions to mitigate the so-called wall instability that forms at the top and bottom of the target [37, 38]. Subsequent experiments with beryllium cushions demonstrated a $10\times$ increase in neutron yield, 60% increase in ion temperature, and an overall $\sim 50\%$ increase in the fuel energy at stagnation [96]. Furthermore, the ratio of x-ray to neutron yield, an indicator for mix due to enhanced Bremsstrahlung radiation and decreased neutron yield, was $3\text{--}5\times$ larger for targets with Al cushions. Mix from the upper cushion was also observed at stagnation by axially-resolved K-shell spectroscopy of a Co coating applied to the surface of that cushion [42]. The source of this mix is attributed to the interaction of the laser preheat with the cushions, which can ablate material into the fuel [53]. While some of this material is likely expelled through the ends of the target during the implosion, these studies clearly demonstrated a significant impact to performance and have resulted in the replacement of aluminum cushions with beryllium.

Deceleration mix arises when the inner interface of the imploding liner begins to stagnate on the high pressure fuel. At this point, the less dense fuel decelerates the heavy liner, making this interface RT unstable. The initial surface roughness of the inside of the target, along with perturbations that have fed-through [58] from MRT in the outside of the target during the implosion can significantly grow during this stage, injecting beryllium mix into the fuel as the liner begins to stagnate. A detailed analysis [96] concluded a typical mix fraction attributed to deceleration mix is 2.4%, which corresponds to roughly 15 nm of beryllium material from the inner liner surface injected into the fuel. For comparison, cushion and window mix (assuming beryllium cushions and a polyimide window) are estimated to be $\sim 1.7\%$ and 0.5% , respectively, in experiments without a distributed phase plate (DPP) optic (see section 4.3). While the window and cushion mix fractions are comparatively low, the duration over which these mixed contaminants radiate is significantly longer than deceleration-mix, and their impact on performance is greater. A detailed

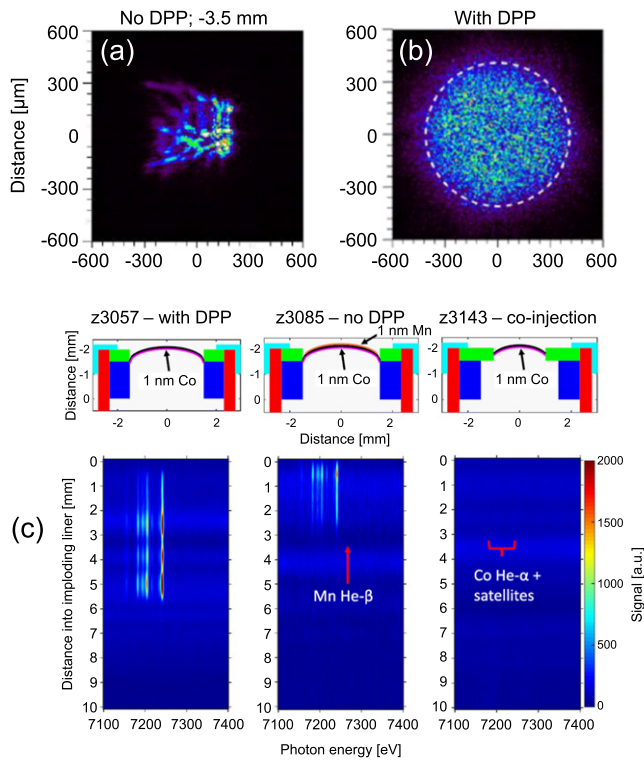


Figure 12. ZBL spatial profiles used in the initial (a) and subsequent (b) MagLIF experiments, the latter which incorporated DPP smoothing. (c) X-ray emission spectra of stagnation columns with Co and Mn coatings applied to the LEH foil as indicated in the diagram. Reproduced from Harvey-Thompson *et al* 2018 *Phys. Plasmas* 25 112705 with the permission of AIP Publishing <https://doi.org/10.1063/1.5050931>.

analysis of the origin and effects of mix on MagLIF can be found in reference [96].

4.3. Laser preheat

The laser preheat protocol has been continuously upgraded since the original MagLIF experiments to better reduce LEH window mix, increase the specific energy (energy per mass) coupled to the fuel, and optimize the propagation length of the laser. Additional experiments and simulations have focused on optimizing the LEH foil thickness and preheat laser power profiles. These experiments are frequently executed using the ZBL and Z-Petawatt (ZPW) [97] lasers in a surrogate chamber [98], at Omega-EP [99, 100], and at $\sim 10\times$ energy scales on the NIF, sufficient for studying ignition-relevant target designs proposed for future facilities [101].

Examination of the spatial profile of the laser in the first MagLIF experiments, shown in figure 12(a), shows a highly non-uniform intensity distribution (note this is acceptable for x-ray backlighting, one of the primary purposes for ZBL). Intense regions in the beam profile can filament the beam and generate laser plasma instabilities (LPI) including stimulated Brillouin scattering in both the window and fuel [41, 102]. Furthermore, modeling this spatial profile using MHD tools is extremely challenging and motivated beam smoothing via a DPP optic. This significantly improved the smoothness of

the beam profile and enabled higher fidelity modeling of laser preheat [41, 42, 103].

As previously discussed, the laser preheat stage can induce mix from the LEH foil. Experiments applying mid-atomic number surface coatings (Mn and Co) to the LEH foil show that this material can be transported into the fuel over a significant fraction of the stagnating plasma column [42]. HYDRA [104] simulations were used to design an 80 J pre-pulse injected 3.5 ns prior to the main pulse to minimize the kinetic energy of LEH foil particles transported into the fuel region (note the unsmoothed preheat protocol also utilized a pre-pulse to disassemble the LEH foil and improve transmission to the fuel). Despite this, experiments still demonstrated increased LEH foil mix propagation and motivated a new preheat protocol referred to as ‘co-injection’, which incorporates a 20–30 J, 2 ns long pre-pulse from the ZPW laser 20 ns before the main preheat from ZBL and allows improved disassembly of the LEH foil (note ZBL is limited to a ~ 7 ns total pulse width). Experimental x-ray emission spectra of stagnation columns shown in figure 12(c) demonstrated that the combination of higher fuel densities with the co-injection protocol significantly reduced emission of spectroscopic Co coatings applied to the LEH foil compared to DPP and no-DPP laser preheats, indicating that window mix can be significantly reduced in MagLIF experiments [42]. Furthermore, co-injection has allowed 1.4 kJ to be coupled to the fuel by using a 20 J co-injected pulse from ZPW with a 0.3 kJ foot (3 ns) and 2.2 kJ main pulse (3 ns) from ZBL. When combined with improvements to the transmission line enabling an increase in current delivered from 16 to 20 MA and magnetic field from 10 to 16 T, the increase in preheat energy coupled from 0.5 to 1.2 kJ resulted in a record primary neutron yield of 1.1×10^{13} , nearly an order of magnitude improvement in performance [25].

Designing a suitable preheat pulse is challenging and requires (1) balancing physical limitations (e.g. foil thickness required to contain the initial fuel pressure), (2) ensuring the laser energy is coupled to the imploding region and does not over-propagate, (3) ensuring sufficient penetration of energy through the LEH foil while balancing LPI and window absorption (the latter can reduce the total energy coupled to the fuel by $\sim 50\%$ or more), and (4) correctly modeling the effects of the pre-imposed axial magnetic field. The magnetic field can redistribute the laser energy in the fuel, increasing filamentation and thus laser intensity and backscatter instabilities. Figure 13 shows a series of 3D HYDRA simulations at $B_z = 0, 10$ and 30 T that couple 2 kJ from a 2.6 kJ laser pulse. As the axial magnetic field is increased, thermal filamentation and associated radial beam expansion are enhanced. These effects tend to increase the deposited energy within the imploding region of the target by shortening the propagation depth. However, they also increase the randomness of the beam propagation that tends to direct the laser filaments toward the liner walls, potentially increasing the chances of liner-fuel mixing [103].

Simulations also suggest that $\sim 72\%$ coupling efficiency (2.7 kJ) to the imploding region is possible [103] when using cryogenically cooled [105] MagLIF targets. Cooling the target to ~ 70 K significantly reduces the initial fuel pressure (4–8 bar

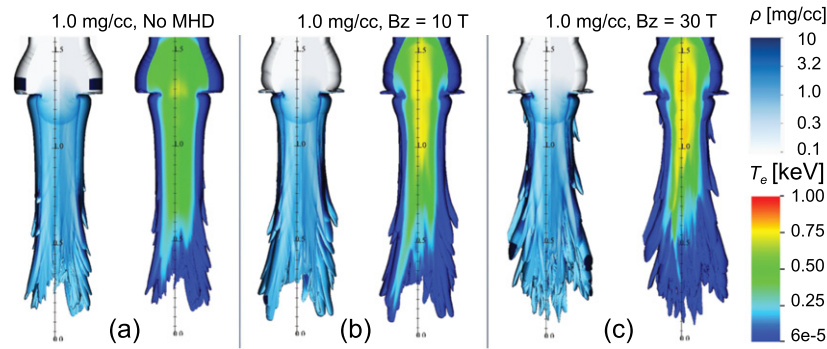


Figure 13. 3D simulations of the laser preheat stage coupling 2 kJ of laser energy to the fuel for 2.6 kJ delivered by the laser for axial magnetic field strengths of (a) 0 T, (b) 10 T and (c) 30 T. Reproduced from Weis *et al* 2021 *Phys. Plasmas* **28** 012705 with the permission of AIP Publishing <https://doi.org/10.1063/5.0029850>.

at room temperature) on the LEH foil required to achieve typical target densities to < 1.7 bar, enabling much thinner (500 nm thick) LEH windows and improved energy coupling to the fuel.

An alternate preheat protocol is being explored where the LEH foil is removed altogether microseconds prior to the main preheat pulse to simultaneously eliminate LEH window mix and increase laser-fuel energy coupling [95]. Two approaches to removing the LEH window have been investigated. In the first approach, a dedicated laser with a spatially tailored beam profile is directed toward the LEH window to perforate certain regions in an asterisk-type pattern (i.e. three intersecting lines) [106]. The fuel pressure opens the resulting flaps outward and away from the main preheat pulse beam path. Recent offline testing using a special optic that converts the ZPW beam profile into the desired asterisk shape has successfully opened LEH windows and enabled ZBL to subsequently preheat the fuel. In the second approach, a small capacitor is used to drive 150–170 A of current through a metallic wire that is partially wrapped around the LEH circumference [107]. The joule heating of the wire melts and weakens the LEH foil, allowing the fuel pressure to preferentially burst the window along the wire. The unmelted region serves as a hinge for the window to open away from the main preheat path to prevent laser-foil interactions during the preheat stage. Experimental results from both approaches are highly encouraging.

4.4. Current delivery and applied magnetic field capability

The current delivered to a MagLIF target and the initial axial magnetic field strength are related by the transmission line requirements to maintain a modest inductance while accommodating Helmholtz-like coils that generate the pre-imposed axial magnetic field [39]. Early MagLIF experiments utilized a high inductance transmission line that allowed coils above and below the target, enabling axial magnetic field uniformity in the target to within 1% for magnetic fields up to 15 T. The static inductance of the transmission line and 10 mm tall target, L , was 7.2 nH within a radius of 55 mm. This high inductance permitted ~ 16 MA to reach the target. Using this transmission line, higher field strengths of 20 T could also be obtained by increasing the number of turns and improving the internal reinforcements in the upper coil, although with a 10% variation in the field strength across the length of the target. Note that

based on LASNEX [108], HYDRA and Gorgon simulations, this variation is not expected to affect performance.

Recently, a new transmission line, shown in figure 14, was designed that enabled ~ 20 MA of current to be applied to 10 mm tall, 4.65 mm ID, AR6 MagLIF targets [25]. Increases to the delivered current were possible due to a reduction of losses in the convolute region [109] and transmission line leading up to the target. The total initial inductance was $L = 5.3$ nH within 55 mm, despite the increase of minimum gap spacing from 3 mm to 5 mm. In some of the first experiments using this transmission line, a single coil was fielded above the target that enabled a 16 T average magnetic field, with a $\sim 30\%$ axial variation in the field due to the lack of a coil situated below the target. Future planned experiments will implement coils above and below the target to enable higher fields (20–30 T) along with improved axial uniformity. Note that the shape of the current pulse, shown in figure 14, was also modified due to the reduced current loss. As mentioned above, recent experiments that implemented simultaneous improvements to the current pulse (16 to 20 MA), axial magnetic field (10 to 16 T) and laser preheat (0.5 to 1.2 kJ) enabled a factor of 10 increase in performance [25].

A novel technique to magnetize MagLIF without external Helmholtz-like coils was designed [110, 111] and implemented [112] on implosion-only Z experiments. This concept, called AutoMag (for auto-magnetizing liners), modifies the liner to include discrete helical conducting paths encapsulated in an insulating material. On Z experiments, the current pulse is modified to include a 1–2 MA, 100–200 ns pre-pulse that flows helically through the liner, generating a pre-compressed axial magnetic field on the interior of the liner that exceeds 100 T, suitable for pre-magnetizing the fuel in integrated MagLIF experiments.

After the pre-pulse, the driver current rises quickly (> 50 kA ns $^{-1}$), inducing strong electric fields in the target and causing flashover of the outer surface of the insulating material. Flashover causes the current in the liner to reorient from helical to primarily axial when the internal field is in the 60–80 T range. Miniature magnetic field probe measurements on Z indicate that a small fraction of the current continues to flow helically, allowing the internal field to continue rising

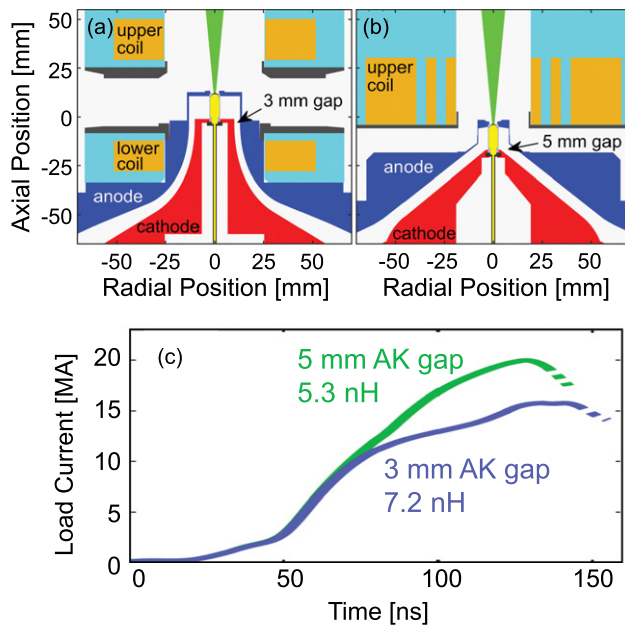


Figure 14. Comparison of MagLIF load hardware of the (a) original and (b) upgraded final transmission line. (c) The peak load current was increased from 16–20 MA by reducing current losses via a simultaneous decrease in the inductance and increase in AK gap distances. Reprinted figure with permission from Gomez *et al* 2020 *Phys. Rev. Lett.* **125** 155002. Copyright 2020 by the American Physical Society <https://doi.org/10.1103/PhysRevLett.125.155002>.

to >150 T after breakdown (albeit with weaker dependence on drive current). Based on non-imploding surrogate experiments on the 1 MA Mykonos accelerator, the internal magnetic field is thought to be supported by eddy currents with resistive decay times much longer than the ~ 100 ns liner implosion time on Z experiments (this work will be presented in a future publication). After flashover, the remainder of the Z electrical energy is delivered to the target via a standard, ~ 100 ns risetime current pulse. This axial current flow magnetically drives a radial implosion of the target, thereby compressing the trapped axial magnetic field inside of the liner internal volume to ~ 1 – 10 kT. While these initial experiments produced pre-compressed fields of >100 T, future experiments could modify the pre-magnetization by controlling the flashover time.

Remarkably, the composite beryllium-dielectric liner showed a high level of cylindrical uniformity as indicated by the radiograph with the highest CR imaged, CR = 5 [112]. This suggests the concept may be a viable technique to produce higher initial axial magnetic fields than realistically attainable with Helmholtz-like coils while reducing the inductance of the transmission line to possibly enable higher electrical currents.

5. High yield and gain in MagLIF

Numerical simulations show that MagLIF has the potential to scale to high yield (7 GJ) and high gain ($\sim 70\times$) with modest convergence ratios (CR = 20–30) [17, 23, 24]. Using a circuit model of a conceptual design for a next generation

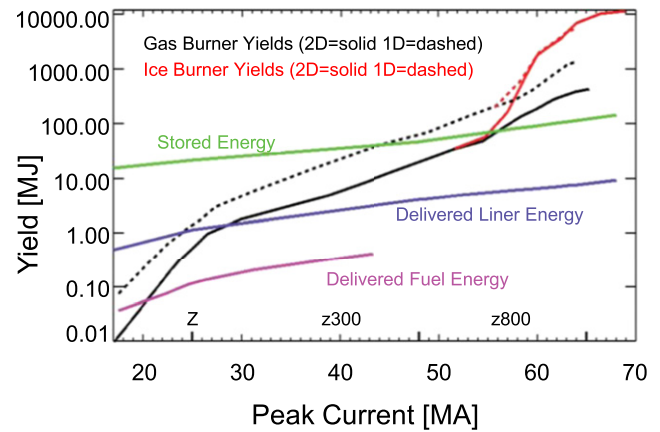


Figure 15. (a) Plot of yield as a function of peak current. At 56 MA, the fusion yield exceeds the stored energy in the capacitor bank. Reproduced from Slutz *et al* 2016 *Phys. Plasmas* **23** 022702 with the permission of AIP Publishing <https://doi.org/10.1063/1.4941100>.

pulsed power machine [113] that couples 65 MA to the target, ‘ice-burner’ models achieve high yields by propagating a burn wave through a thin annulus of DT ice inside of the liner. Even without the layer of DT ice, the energy produced in ‘gas-burner’ simulations surpasses the energy stored in the capacitor bank when the current exceeds 56 MA. Figure 15 shows optimized yields from 2D LASNEX simulations [24] for both ‘gas burner’ and ‘ice burner’ approaches, along with the energy delivered to the fuel and liner and total stored energy in the pulsed power machine’s capacitor bank versus peak current. The scaling curves in figure 15 were obtained by following an optimization approach, in which the input parameters defining a MagLIF target were varied to maximize the neutron yield at a given peak current (note the axial magnetic field was limited to ≤ 30 T, constrained by physical limitations of the external Helmholtz-like coils). Interestingly, the optimal axial magnetic field for gas burners decreases from 30 T for currents above 53 MA, with an optimal value of 10 T at 60 MA. In these simulations, the blast wave resulting from laser preheat compresses some of the DT fuel against the liner. Sufficiently low axial fields allow the burn wave from the hotter regions of the fuel to radially propagate into this colder region, offsetting the benefits of decreased thermal conduction losses. These results represent an optimistic scenario on how a MagLIF target could perform at higher electrical currents. Additional simulations investigating the scaling of performance with the current pulse risetime may be found in reference [114].

Recently, an alternative approach was proposed to ‘conservatively’ scale present-day MagLIF experiments to higher peak currents [33]. Instead of maximizing the yield as in the optimization approach described above, scaling strategies are identified that preserve much of the physics regimes already known or being studied on the Z machine today. In essence, this is done by identifying a simple model that captures most of the physics relevant to MagLIF (similar to that in section 2) and then identifying the key dimensionless parameters that characterize the model. These parameters describe the physics concerning the target-implosion dynamics, hydrodynamic instabilities and mix,

energy-loss mechanisms, transport physics, laser–plasma interactions, and others. When the peak current is varied, the experimental input parameters for a MagLIF target are scaled in such a way that the maximum number of dimensionless parameters are conserved. By doing so, this ‘conservative’ scaling paradigm seeks to reduce the risk in the performance of a potential scaled-up MagLIF platform by minimizing extrapolation away from the most robustly studied parameter space accessible to present-day experiments. It is important to note that, presently, this analytic-based scaling treatment does not account for alpha-particle heating, indicating that these yield scalings represent a lower-bound prediction of performance. Having said this, numerical simulations of self-similarly scaled targets do indicate a robust alpha-heating regime is attainable so that the resulting predictions in yield are higher than analytically indicated. These simulations will be presented in future publications.

Designs for a next-generation 60 MA pulsed-power facility [113] consider current rise-times of ~ 100 ns (similar to the present-day Z facility) and ~ 300 ns. To account for these possibilities, two broad families of scaling approaches were considered in reference [33]: the pressure–velocity conserving (PVC) and implosion-time conserving (ITC) scaling approaches. The PVC approach attempts to preserve the absolute values and time histories of all intrinsic hydrodynamic variables, including the fuel pressure, magnetic drive pressure, and the liner velocity. This scaling approach is similar to the ‘hydro-equivalent scaling’ paradigm that is presently championed by the laser ICF community [115]. Analytical estimates using this scaling approach show that the neutron yield scales with current as $Y \simeq [I_{\max}^4, I_{\max}^5]$, where the bracketed values bound the possible scaling exponents for the broader PVC family of scaling paths without accounting for alpha-heating (see reference [33] for more details). The ITC approach attempts to preserve the implosion time for MagLIF at higher peak currents. Similarly to the PVC scaling strategies, the ITC approach preserves self-similar implosions and conserves a large number of dimensionless parameters that characterize the salient MagLIF-related physics. Analytical estimates show that the no-alpha neutron yield scales with current as $Y \simeq [I_{\max}^{3.29}, I_{\max}^{4.57}]$, where again the bracketed values bound the possible scaling paths for the ITC approach.

It is worth noting that the PVC scaling strategies show a stronger overall scaling in yield. This result is primarily driven by the larger target heights needed to maintain end losses with the longer implosion times of PVC targets. However, due to the increased target volume, significantly more preheat energy is required. In terms of the yield per-unit-length (ratio of yield to target length), the ITC scaling strategies show more favorable scaling because they achieve higher stagnation pressures when scaling up in current. Due to their smaller fuel volumes, ITC targets require less preheat energies when compared to PVC targets driven at the same peak current.

In figure 16, the yield vs peak current is plotted for the various scaling approaches. The ‘optimized’ scaling curves, represented by the green and red curves, suggest that MagLIF can reach MJ-yields when driven to around 40 MA even without considering the boost in yield due to alpha-heating. The

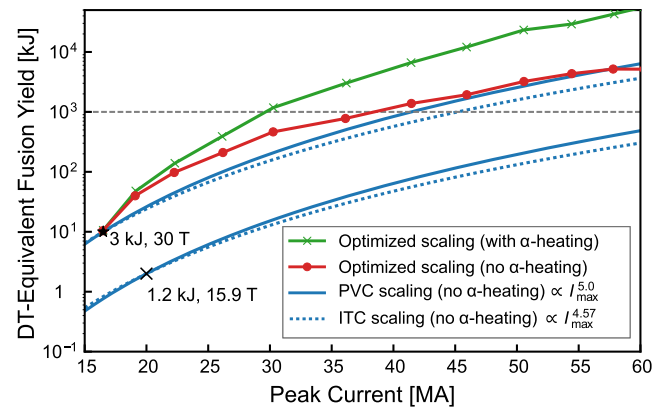


Figure 16. Comparison of the various scaling approaches to higher peak currents for the MagLIF platform. The green and red curves indicate the ‘optimized’ scaling curves driven similarly to those described in reference [24]. The blue curves correspond to the conservative scaling paths discussed in reference [33]. Note only the ‘radiation-conserving’ scaling strategies are shown. The black ‘x’ marker shows where current MagLIF experiments sit in terms of DT-equivalent neutron yield [25], while the black ‘star’ marker indicates an aspirational MagLIF target that will require higher preheat energies and stronger external magnetic fields to achieve almost an order of magnitude increase in neutron yield.

difference between the green and red curves at higher currents indicates that a robust alpha-heating regime can be achieved. It is worth noting that these curves were obtained by limiting the external magnetic field to 30 T and by assuming a constant aspect ratio of 6 for all scaled-up targets. Similar versions of these curves where the aspect ratio is decreased to mitigate the effects of MRT have been obtained [116]. Overall, the ‘optimized’ scaling curves represent an optimistic scenario for the MagLIF platform. For reference, the best performing experiments are within a factor of 2–3 \times of clean 2D simulations.

Figure 16 also illustrates the potential yields that can be achieved when ‘conservatively’ scaling MagLIF. Since such scaling enforces that the same physics regimes are maintained in scaled-up targets as in present-day experiments, the scaling exponents of these curves tend to be slightly reduced compared to their ‘optimized’ counterparts. It is important to note that these theoretical curves do not take into account the yield enhancement from alpha-particle heating and should be considered as a lower bound prediction of performance. However, analytic calculations suggest that a robust self-heating regime can be achieved based on the favorable scaling of the Lawson ignition parameter [33].

When conservatively scaling MagLIF, the baseline target (i.e. the target from which the scaling is done) determines the target requirements and estimated performance at higher currents. Figure 16 shows two baseline targets. The first is a present-day MagLIF target (20 MA, 1.2 kJ preheat, 16 T) and the second is an aspirational, higher performing MagLIF configuration (16 MA, 3 kJ preheat, 30 T) that is calculated to be scalable to multi-MJ yields. A near-term objective is to experimentally test configurations predicted to scale to these high yields.

Experiments on Z are underway to test the underlying principles of scaling MagLIF. Due to energy limitations of the Z-beamlet laser, it is presently difficult to experimentally assess the ‘optimization’ scaling approach; however, the ITC conservative scaling approach can be tested by self-similarly scaling from 14 MA to 20 MA following the prescriptions outlined in reference [33]. These experiments will test predictions for the scaling of neutron yield, ion temperature, morphology of the stagnation column and x-ray bang-time.

6. Fusion energy

Experiments in 2013 established the MagLIF concept as the first demonstration of MIF in the laboratory [18]. This proof-of-concept has played an important role in motivating the ARPA-E ALPHA fusion program focused on advancing MIF-relevant, intermediate-density fusion approaches (i.e. between ICF and MCF) with a direct emphasis on lower-cost pathways to commercially viable fusion energy [117–120]. While MagLIF research at Sandia National Laboratories is primarily funded by the United States Inertial Confinement Fusion program and mainly interested in generating single shot, multi-MJ fusion yields for the Stockpile Stewardship Program [121], the possibility of high gain is encouraging from a fusion energy perspective [16]. To quantify this, we follow reference [23] and define the gain, G , as the ratio of fusion yield to the energy delivered to the imploding liner, so that the minimum gain required for inertial fusion energy is given by

$$G\eta_E f_{RP}\eta_D = 1, \quad (16)$$

where $\eta_E \simeq 0.4$ is the efficiency of the power plant at converting fusion to electrical energy, $f_{RP} \simeq 0.25$ is the fraction of generated power available after re-directing energy to operate the power plant, and η_D is the efficiency of the driver at converting wall-plug energy to the liner. Magnetic direct drive is relatively efficient, with as high as 20% conversion efficiency, thus setting the required gain to be at least $G = 50$. Interestingly, optimized 2D simulations of ice-burner targets show gains exceeding 70 may be possible at 65 MA peak currents, suggesting MagLIF at currents attainable on a next generation machine may already be feasible for demonstrating its suitability as an energy producing source. Furthermore, success at these higher currents would likely motivate investigation of larger gains on subsequent facilities with even higher currents. Note the existing Z machine delivers $\sim 5\%$ of the stored energy in the capacitor bank to the liner; however, it was not designed to optimize energy coupling to MagLIF targets. Future fusion producing plants would therefore require more efficient drivers (or higher gains) to compensate.

Practical implementation of MagLIF as an energy source will be challenging [121]. First, Z experiments generate a destructive post-shot explosion (even in the absence of fusion yields) that destroys the metallic transmission line that delivers current to the target, limiting present-day operations to a single shot per day. Clever engineering solutions, such as

recyclable transmission lines [122], must be implemented to achieve high repetition rates. Gigajoule producing targets would additionally unleash a tremendous number of neutrons that could adversely affect pulsed power components and activate materials to potentially hazardous levels. This could be mitigated by neutron-absorbing blankets or by placing the target and destructible section of the transmission line sufficiently far from pulsed power components. Finally, extraction of the fusion energy itself must be addressed. This could be accomplished in a manner similar to that described in references [123, 124], where 14 MeV neutrons are stopped in a neutron-absorbing blanket surrounding the target, converting this material into a plasma suitable for electricity extraction via an MHD generator (e.g. a Compact Fusion Advanced Rankine-II reactor [123]).

The most important step to establish MagLIF as a fusion energy source is to first demonstrate its capability to produce high gains. While subsequent efforts could address the engineering challenges, our present efforts in MagLIF are directed toward demonstrating the fundamental physics and possibility of attaining significant fusion gains on larger-scale facilities via current scaling studies.

7. Conclusions

The magneto inertial fusion concept MagLIF offers a promising path to high fusion yield. Experiments have demonstrated its potential viability by producing fusion-relevant temperatures, significant neutron production ($> 10^{13}$ DD-produced neutrons), and magnetic trapping of charged fusion products. Numerical simulations demonstrate scaling to gigajoule yields may be possible at currents of 65 MA by propagating the burn wave into a layer of DT ice inside the liner. With gains of order 70, MagLIF has the potential to be a viable source of fusion energy.

MagLIF research over the past decade has focused on demonstrating sufficient stability in the imploding liner, mitigating mix arising from the laser preheat interaction with the LEH foil and cushions, optimizing the laser preheat stage and improving the transmission line to simultaneously improve current coupling and enable increased pre-applied axial magnetic fields. Improvements in these areas have allowed us to increase the neutron yield by a factor of 10 by increasing the applied axial magnetic field from 10 to 16 T, the laser preheat energy coupled from 0.5 to 1.2 kJ, and current delivered to the target from 16 to 20 MA. With further improvements in applied axial magnetic field, laser preheat and current delivery, simulations show DT-equivalent yields of ~ 100 kJ are possible on Z.

Future research in MagLIF will focus on both improving the input parameters and demonstrating the physics of scaling across currents presently attainable on the Z machine to improve confidence in generating significant fusion gains on larger scale facilities. Surmounting this scientific difficulty remains the first obstacle toward harnessing a MIF-energy producing system.

Acknowledgments

Sandia National Laboratories is a multimission laboratory managed and operated by National Technology and Engineering Solutions of Sandia, LLC, a wholly owned subsidiary of Honeywell International Inc., for the US Department of Energy's National Nuclear Security Administration under Contract DE-NA0003525. This paper describes objective technical results and analysis. Any subjective views or opinions that might be expressed in the paper do not necessarily represent the views of the US Department of Energy or the United States Government.

ORCID iDs

D.A. Yager-Elorriaga  <https://orcid.org/0000-0001-6110-1700>
 M.R. Gomez  <https://orcid.org/0000-0002-1967-7113>
 D.E. Ruiz  <https://orcid.org/0000-0002-2321-3274>
 P.F. Schmit  <https://orcid.org/0000-0002-9709-7333>
 M.R. Weis  <https://orcid.org/0000-0003-0061-5323>
 C.E. Myers  <https://orcid.org/0000-0003-4539-8406>
 J.R. Fein  <https://orcid.org/0000-0002-6460-9873>
 B.R. Galloway  <https://orcid.org/0000-0002-4230-5561>
 M. Geissel  <https://orcid.org/0000-0002-6207-7615>
 M.E. Glinsky  <https://orcid.org/0000-0003-2493-3326>
 S.B. Hansen  <https://orcid.org/0000-0002-1886-9770>
 W.E. Lewis  <https://orcid.org/0000-0003-0509-8353>
 G.A. Shipley  <https://orcid.org/0000-0002-0536-4001>
 D.J. Ampleford  <https://orcid.org/0000-0002-3742-2421>
 K.J. Peterson  <https://orcid.org/0000-0001-6202-4292>
 D.B. Sinars  <https://orcid.org/0000-0001-5547-3532>

References

- [1] Lindl J. 1995 Development of the indirect-drive approach to inertial confinement fusion and the target physics basis for ignition and gain *Phys. Plasmas* **2** 3933
- [2] Nuckolls J., Wood L., Thiessen A. and Zimmerman G. 1972 Laser compression of matter to super-high densities: thermonuclear (CTR) applications *Nature* **239** 139
- [3] Meezan N.B. *et al* 2010 National ignition campaign Hohlraum energetics *Phys. Plasmas* **17** 056304
- [4] Perkins L.J., Betti R., LaFortune K.N. and Williams W.H. 2009 Shock ignition: a new approach to high gain inertial confinement fusion on the National Ignition Facility *Phys. Rev. Lett.* **103** 045004
- [5] Lindemuth I.R. and Widner M.M. 1991 Magnetohydrodynamic behavior of thermonuclear fuel in a preconditioned electron beam imploded target *Phys. Fluids* **24** 746
- [6] Lindemuth I.R. and Kirkpatrick R.C. 1983 Parameter space for magnetized fuel targets in inertial confinement fusion *Nucl. Fusion* **23** 263
- [7] Hasegawa A., Daido H., Fujita M., Mima K., Murakami M., Nakai S., Nishihara K., Terai K. and Yamanaka C. 1986 Magnetically insulated inertial fusion: a new approach to controlled thermonuclear fusion *Phys. Rev. Lett.* **56** 139
- [8] Basko M.M., Kemp A.J. and Meyer-ter-Vehn J. 2002 Ignition conditions for magnetized target fusion in cylindrical geometry *Nucl. Fusion* **40** 59
- [9] Hsu S.C. 2009 Technical summary of the first US Plasma Jet Workshop *J. Fusion Energy* **28** 246
- [10] Degnan J.H. *et al* 2013 Recent magneto-inertial fusion experiments on the field reversed configuration heating experiment *Nucl. Fusion* **53** 093003
- [11] Matzen M.K. *et al* 2005 Pulsed-power-driven high energy density physics and inertial confinement fusion research *Phys. Plasmas* **12** 055503
- [12] Savage M.E., LeChien K., Stygar W., Maenchen J., McDaniel D. and Struve K. 2008 Overview and status of the upgraded Z pulsed power driver *Proc. 2008 IEEE Int. Power Modulators and High Voltage Conf.* (Las Vegas, NV, USA 27-31 May 2008) p 93
- [13] Sinars D.B. *et al* 2020 Review of pulsed power-driven high energy density physics research on Z at Sandia *Phys. Plasmas* **27** 070501
- [14] McBride R.D. *et al* 2018 A primer on pulsed power and linear transformer drivers for high energy density physics applications *IEEE Trans. Plasma Sci.* **46** 3928
- [15] Slutz S.A., Herrmann M.C., Vesey R.A., Sefkow A.B., Sinars D.B., Rovang D.C., Peterson K.J. and Cuneo M.E. 2010 Pulsed-power-driven cylindrical liner implosions of laser preheated fuel magnetized with an axial field *Phys. Plasmas* **17** 056303
- [16] Cuneo M.E. *et al* 2012 Magnetically driven implosions for inertial confinement fusion at Sandia National Laboratories *IEEE Trans. Plasma Sci.* **40** 3222
- [17] Sefkow A.B., Slutz S.A., Koning J.M., Marinak M.M., Peterson K.J., Sinars D.B. and Vesey R.A. 2014 Design of magnetized liner inertial fusion experiments using the Z facility *Phys. Plasmas* **21** 072711
- [18] Gomez M.R. *et al* 2014 Experimental demonstration of fusion-relevant conditions in magnetized liner inertial fusion *Phys. Rev. Lett.* **113** 155003
- [19] Gomez M.R. *et al* 2015 Demonstration of thermonuclear conditions in magnetized liner inertial fusion experiments *Phys. Plasmas* **22** 056306
- [20] Schmit P.F. *et al* 2014 Understanding fuel magnetization and mix using secondary nuclear reactions in magneto-inertial fusion *Phys. Rev. Lett.* **113** 155004
- [21] Knapp P.F. *et al* 2015 Effects of magnetization on fusion product trapping and secondary neutron spectra *Phys. Plasmas* **22** 056312
- [22] Hansen S.B. *et al* 2015 Diagnosing magnetized liner inertial fusion experiments on Z *Phys. Plasmas* **22** 056313
- [23] Slutz S.A. and Vesey R.A. 2012 High-gain magnetized inertial fusion *Phys. Rev. Lett.* **108** 025003
- [24] Slutz S.A., Stygar W.A., Gomez M.R., Peterson K.J., Sefkow A.B., Sinars D.B., Vesey R.A., Campbell E.M. and Betti R. 2016 Scaling magnetized liner inertial fusion on Z and future pulsed-power accelerators *Phys. Plasmas* **23** 022702
- [25] Gomez M.R. *et al* 2020 Performance scaling in magnetized liner inertial fusion experiments *Phys. Rev. Lett.* **125** 155002
- [26] Davies J.R., Barnak D.H., Betti R., Campbell E.M., Chang P.-Y., Sefkow A.B., Peterson K.J., Sinars D.B. and Weis M.R. 2017 Laser-driven magnetized liner inertial fusion *Phys. Plasmas* **24** 062701
- [27] Barnak D.H. *et al* 2017 Laser-driven magnetized liner inertial fusion on OMEGA *Phys. Plasmas* **24** 056310
- [28] Hansen E.C. *et al* 2018 Measuring implosion velocities in experiments and simulations of laser-driven cylindrical implosions on the OMEGA laser *Plasma Phys. Control. Fusion* **60** 054014
- [29] Davies J.R. *et al* 2018 Laser entrance window transmission and reflection measurements for preheating in magnetized liner inertial fusion *Phys. Plasmas* **25** 062704
- [30] Davies J.R., Barnak D.H., Betti R., Campbell E.M., Glebov V.Y., Hansen E.C., Knauer J.P., Peebles J.L. and Sefkow A.B. 2019 Inferring fuel areal density from secondary

- neutron yields in laser-driven magnetized liner inertial fusion *Phys. Plasmas* **26** 022706
- [31] Hansen E.C. *et al* 2020 Neutron yield enhancement and suppression by magnetization in laser-driven cylindrical implosions *Phys. Plasmas* **27** 062703
- [32] Atzeni S. and Meyer-ter Vehn J. 2009 *The Physics of Inertial Fusion: Beam-Plasma Interaction, Hydrodynamics, Hot Dense Matter (International Series of Monographs on Physics)* (Oxford: Oxford University Press)
- [33] Schmit P.F. and Ruiz D.E. 2020 A conservative approach to scaling magneto-inertial fusion concepts to larger pulsed-power drivers *Phys. Plasmas* **27** 062707
- [34] McBride R.D. and Slutz S.A. 2015 A semi-analytic model of magnetized liner inertial fusion *Phys. Plasmas* **22** 052708
- [35] W.E. Lewis 2021 Deep-learning-enabled Bayesian inference of fuel magnetization in magnetized liner inertial fusion *Phys. Plasmas* **28** 092701
- [36] McBride R.D. *et al* 2016 Exploring magnetized liner inertial fusion with a semi-analytic model *Phys. Plasmas* **23** 012705
- [37] McBride R.D. *et al* 2013 Beryllium liner implosion experiments on the Z accelerator in preparation for magnetized liner inertial fusion *Phys. Plasmas* **20** 056309
- [38] Awe T.J. *et al* 2013 Observations of modified three-dimensional instability structure for imploding Z-pinch liners that are premagnetized with an axial field *Phys. Rev. Lett.* **111** 235005
- [39] Rovang D.C. *et al* 2014 Pulsed-coil magnet systems for applying uniform 10–30 T fields to centimeter-scale targets on Sandia's Z facility *Rev. Sci. Instrum.* **85** 124701
- [40] Rambo P.K. *et al* 2005 Z-beamlet: a multikilojoule, terawatt-class laser system *Appl. Opt.* **44** 2421
- [41] Geissel M. *et al* 2018 Minimizing scatter-losses during pre-heat for magneto-inertial fusion targets *Phys. Plasmas* **25** 022706
- [42] Harvey-Thompson A.J. *et al* 2018 Diagnosing and mitigating laser preheat induced mix in MagLIF *Phys. Plasmas* **25** 112705
- [43] Awe T.J. *et al* 2014 Modified helix-like instability structure on imploding z-pinch liners that are pre-imposed with a uniform axial magnetic field *Phys. Plasmas* **21** 056303
- [44] Glinsky M.E. *et al* 2020 Quantification of MagLIF morphology using the Mallat scattering transformation *Phys. Plasmas* **27** 112703
- [45] Hahn K.D. *et al* 2016 Fusion-neutron measurements for magnetized liner inertial fusion experiments on the Z accelerator *J. Phys.: Conf. Ser.* **717** 012020
- [46] Hansen S.B., Harding E.C., Knapp P.F., Gomez M.R., Nagayama T. and Bailey J.E. 2017 Changes in the electronic structure of highly compressed iron revealed by x-ray fluorescence lines and absorption edges *High Energy Density Phys.* **24** 39
- [47] Hansen S.B., Harding E.C., Knapp P.F., Gomez M.R., Nagayama T. and Bailey J.E. 2018 Fluorescence and absorption spectroscopy for warm dense matter studies and ICF plasma diagnostics *Phys. Plasmas* **25** 056301
- [48] Ampleford D.J. *et al* 2018 One dimensional imager of neutrons on the Z machine *Rev. Sci. Instrum.* **89** 101132
- [49] Ruiz C.L. *et al* 2019 Novel beryllium-scintillator, neutron-fluence detector for magnetized liner inertial fusion experiments *Phys. Rev. Accel. Beams* **22** 042901
- [50] Ruiz C.L., Fehl D.L., Chandler G.A., Cooper G., Jones B., Styron J.D. and Torres J. 2020 Multichannel, triaxial, neutron time-of-flight diagnostic for experiments at the Z facility *Phys. Rev. Accel. Beams* **23** 020401
- [51] Webb T.J., Ampleford D., Ball C.R., Gomez M.R., Lake P.W., Maurer A. and Presura R. 2021 A time-resolved, in-chamber x-ray pinhole imager for Z *Rev. Sci. Instrum.* **92** 033512
- [52] Anderson O.A., Baker W.R., Colgate S.A., Ise J. and Pyle R.V. 1958 Neutron production in linear deuterium pinches *Phys. Rev.* **110** 1375
- [53] Gomez M.R. *et al* 2019 Assessing stagnation conditions and identifying trends in magnetized liner inertial fusion *IEEE Trans. Plasma Sci.* **47** 2081
- [54] Rayleigh L. 1883 Investigation of the character of the equilibrium of an incompressible heavy fluid of variable density *Proc. Lond. Math. Soc.* **14** 170
- [55] Taylor G.I. 1950 The instability of liquid surfaces when accelerated in a direction perpendicular to their planes: I *Proc. R. Soc. A* **201** 192
- [56] Harris E.G. 1962 Rayleigh–Taylor instabilities of a collapsing cylindrical shell in a magnetic field *Phys. Fluids* **5** 1057
- [57] Chandrasekhar S. 1961 *Hydrodynamic and Hydromagnetic Stability* (Oxford: Clarendon)
- [58] Lau Y.Y., Zier J.C., Rittersdorf I.M., Weis M.R. and Gilgenbach R.M. 2011 Anisotropy and feedthrough in magneto-Rayleigh–Taylor instability *Phys. Rev. E* **83** 066405
- [59] Weis M.R., Zhang P., Lau Y.Y., Schmit P.F., Peterson K.J., Hess M. and Gilgenbach R.M. 2015 Coupling of sausage, kink, and magneto-Rayleigh–Taylor instabilities in a cylindrical liner *Phys. Plasmas* **22** 032706
- [60] Velikovich A.L. and Schmit P.F. 2015 Bell–Plesset effects in Rayleigh–Taylor instability of finite-thickness spherical and cylindrical shells *Phys. Plasmas* **22** 122711
- [61] Ruiz D.E. 2020 On a variational formulation of the weakly nonlinear magnetic Rayleigh–Taylor instability *Phys. Plasmas* **27** 022121
- [62] Sinars D.B. *et al* 2010 Measurements of magneto-Rayleigh–Taylor instability growth during the implosion of initially solid Al tubes driven by the 20 MA, 100 ns Z facility *Phys. Rev. Lett.* **105** 185001
- [63] Sinars D.B. *et al* 2011 Measurements of magneto-Rayleigh–Taylor instability growth during the implosion of initially solid metal liners *Phys. Plasmas* **18** 056301
- [64] McBride R.D. *et al* 2012 Penetrating radiography of imploding and stagnating beryllium liners on the Z accelerator *Phys. Rev. Lett.* **109** 135004
- [65] Oreshkin V.I. 2008 Thermal instability during an electrical wire explosion *Phys. Plasmas* **15** 092103
- [66] Peterson K.J. *et al* 2012 Electrothermal instability growth in magnetically driven pulsed power liners *Phys. Plasmas* **19** 092701
- [67] Peterson K.J., Yu E.P., Sinars D.B., Cuneo M.E., Slutz S.A., Koning J.M., Marinak M.M., Nakhleh C. and Herrmann M.C. 2013 Simulations of electrothermal instability growth in solid aluminum rods *Phys. Plasmas* **20** 056305
- [68] Peterson K.J. *et al* 2014 Electrothermal instability mitigation by using thick dielectric coatings on magnetically imploded conductors *Phys. Rev. Lett.* **112** 135002
- [69] Roussikh A.G., Oreshkin V.I., Chaikovskiy S.A., Labetskaya N.A., Shishlov A.V., Beilis I.I. and Baksht R.B. 2008 Study of the strata formation during the explosion of a wire in vacuum *Phys. Plasmas* **15** 102706
- [70] Pecover J.D. and Chittenden J.P. 2015 Instability growth for magnetized liner inertial fusion seeded by electro-thermal, electro-choric, and material strength effects *Phys. Plasmas* **22** 102701
- [71] Hutchinson T.M., Awe T.J., Bauer B.S., Yates K.C., Yu E.P., Yelton W.G. and Fuelling S. 2018 Experimental observation of the stratified electrothermal instability on aluminum with thickness greater than a skin depth *Phys. Rev. E* **97** 053208
- [72] Steiner A.M., Campbell P.C., Yager-Elorriaga D.A., Cochrane K.R., Mattsson T.R., Jordan N.M., McBride R.D., Lau Y.Y. and Gilgenbach R.M. 2018 The electro-thermal stability

- of tantalum relative to aluminum and titanium in cylindrical liner ablation experiments at 550 kA *Phys. Plasmas* **25** 032701
- [73] Steiner A.M., Campbell P.C., Yager-Elorriaga D.A., Jordan N.M., McBride R.D., Lau Y.Y. and Gilgenbach R.M. 2018 The electrothermal instability on pulsed power ablations of thin foils *IEEE Trans. Plasma Sci.* **46** 3753
- [74] Awe T.J., Yu E.P., Yates K.C., Yelton W.G., Bauer B.S., Hutchinson T.M., Fuelling S. and McKenzie B.B. 2017 On the evolution from micrometer-scale inhomogeneity to global overheated structure during the intense joule heating of a z-pinch rod *IEEE Trans. Plasma Sci.* **45** 584
- [75] Yu E.P., Awe T.J., Cochrane K.R., Yates K.C., Hutchinson T.M., Peterson K.J. and Bauer B.S. 2020 Use of hydrodynamic theory to estimate electrical current redistribution in metals *Phys. Plasmas* **27** 052703
- [76] Yu E., Awe T., Bauer B., Yates K., Yelton W.G., Hutchinson T., Fuelling S., McKenzie B.B. and Peterson K. 2016 *Tech. Rep.* Albuquerque, NM Sandia National Laboratories (SNL-NM)
- [77] Awe T.J. *et al* 2016 Experimental demonstration of the stabilizing effect of dielectric coatings on magnetically accelerated imploding metallic liners *Phys. Rev. Lett.* **116** 065001
- [78] Ampleford D.J. *et al* 2021 Improved morphology and reproducibility of magnetized liner inertial fusion experiments (in preparation).
- [79] Yager-Elorriaga D.A., Zhang P., Steiner A.M., Jordan N.M., Campbell P.C., Lau Y.Y. and Gilgenbach R.M. 2016 Discrete helical modes in imploding and exploding cylindrical, magnetized liners *Phys. Plasmas* **23** 124502
- [80] Yager-Elorriaga D.A., Zhang P., Steiner A.M., Jordan N.M., Lau Y.Y. and Gilgenbach R.M. 2016 Seeded and unseeded helical modes in magnetized, non-imploding cylindrical liner-plasmas *Phys. Plasmas* **23** 101205
- [81] Ryutov D.D., Awe T.J., Hansen S.B., McBride R.D., Peterson K.J., Sinars D.B. and Slutz S.A. 2014 Effect of axial magnetic flux compression on the magnetic Rayleigh–Taylor instability (theory) *AIP Conf. Proc.* **1639** 63
- [82] Seyler C.E., Martin M.R. and Hamlin N.D. 2018 Helical instability in MagLIF due to axial flux compression by low-density plasma *Phys. Plasmas* **25** 062711
- [83] Yu E.P. 2021 private communication.
- [84] Sefkow A.B. 2016 *Tech. Rep.* Albuquerque, NM Sandia National Laboratories (SNL-NM)
- [85] Yager-Elorriaga D.A., Steiner A.M., Patel S.G., Jordan N.M., Lau Y.Y. and Gilgenbach R.M. 2015 Technique for fabrication of ultrathin foils in cylindrical geometry for liner-plasma implosion experiments with sub-megaampere currents *Rev. Sci. Instrum.* **86** 113506
- [86] Yager-Elorriaga D.A., Lau Y.Y., Zhang P., Campbell P.C., Steiner A.M., Jordan N.M., McBride R.D. and Gilgenbach R.M. 2018 Evolution of sausage and helical modes in magnetized thin-foil cylindrical liners driven by a z-pinch *Phys. Plasmas* **25** 056307
- [87] Atoyan L., Hammer D.A., Kusse B.R., Byvank T., Cahill A.D., Greenly J.B., Pikuz S.A. and Shelkovenko T.A. 2016 Helical plasma striations in liners in the presence of an external axial magnetic field *Phys. Plasmas* **23** 022708
- [88] Knapp P.F. *et al* 2017 Direct measurement of the inertial confinement time in a magnetically driven implosion *Phys. Plasmas* **24** 042708
- [89] Springer P.T. *et al* 2018 A 3D dynamic model to assess the impacts of low-mode asymmetry, aneurysms and mix-induced radiative loss on capsule performance across inertial confinement fusion platforms *Nucl. Fusion* **59** 032009
- [90] Awe T.J. *et al* 2021 Seeding the explosion of a high-current-density conductor in a controlled manner through the addition of micron-scale surface defects *Phys. Plasmas* **28** 072104
- [91] Schmit P.F., Velikovich A.L., McBride R.D. and Robertson G.K. 2016 Controlling Rayleigh–Taylor instabilities in magnetically driven solid metal shells by means of a dynamic screw pinch *Phys. Rev. Lett.* **117** 205001
- [92] Campbell P.C. *et al* 2020 Stabilization of liner implosions via a dynamic screw pinch *Phys. Rev. Lett.* **125** 035001
- [93] Shipley G.A., Jennings C.A. and Schmit P.F. 2019 Design of dynamic screw pinch experiments for magnetized liner inertial fusion *Phys. Plasmas* **26** 102702
- [94] Ruiz D.E., Schmit P.F., Yager-Elorriaga D.A. and Weis M.R. 2021 Scaling magneto-inertial fusion targets with radius and mass (in preparation).
- [95] Slutz S.A. *et al* 2018 Enhancing performance of magnetized liner inertial fusion at the Z facility *Phys. Plasmas* **25** 112706
- [96] Knapp P.F. *et al* 2019 Origins and effects of mix on magnetized liner inertial fusion target performance *Phys. Plasmas* **26** 012704
- [97] Schwarz J., Rambo P., Geissel M., Edens A., Smith I., Brambrink E., Kimmel M. and Atherton B. 2008 Activation of the z-petawatt laser at Sandia National Laboratories *J. Phys.: Conf. Ser.* **112** 032020
- [98] Harvey-Thompson A.J. *et al* 2019 Constraining preheat energy deposition in MagLIF experiments with multi-frame shadowgraphy *Phys. Plasmas* **26** 032707
- [99] Harvey-Thompson A.J. *et al* 2015 Diagnosing laser-preheated magnetized plasmas relevant to magnetized liner inertial fusion *Phys. Plasmas* **22** 122708
- [100] Harvey-Thompson A.J. *et al* 2020 The effect of laser entrance hole foil thickness on MagLIF-relevant laser preheat *Phys. Plasmas* **27** 113301
- [101] Pollock B. *et al* 2019 *61st Annual Meeting of the APS Division of Plasma Physics* (Fort Lauderdale, FL, USA 21–25 October, 2019) pp 6–007 (<http://meetings.aps.org/link/BAPS.2019.DPP.TO6.7>)
- [102] Geissel M. *et al* 2016 Nonlinear laser-plasma interaction in magnetized liner inertial fusion *SPIE LASE* vol 9731 (San Francisco, CA, USA 28 August–1 September, 2016) (p 973100)
- [103] Weis M.R., Harvey-Thompson A.J. and Ruiz D.E. 2021 Scaling laser preheat for MagLIF with the z-beamlet laser *Phys. Plasmas* **28** 012705
- [104] Koning J., Kerbel G. and Marinak M. 2011 *53rd Annual Meeting of the APS Division of Plasma Physics* (Salt Lake City, UT, USA 14–18 November, 2011) pp 9–115 (<http://meetings.aps.org/link/BAPS.2011.DPP.GP9.115>)
- [105] Awe T.J., Shelton K.P., Sefkow A.B., Lamppa D.C., Baker J.L., Rovang D.C. and Robertson G.K. 2017 Development of a cryogenically cooled platform for the magnetized liner inertial fusion (MagLIF) program *Rev. Sci. Instrum.* **88** 093515
- [106] Galloway B.R. *et al* 2021 Lasergate: a windowless gas target for enhanced laser preheat in magnetized liner inertial fusion *Phys. Plasmas* (in press).
- [107] Miller S.M. *et al* 2020 A pulsed-power implementation of ‘laser gate’ for increasing laser energy coupling and fusion yield in magnetized liner inertial fusion (MagLIF) *Rev. Sci. Instrum.* **91** 063507
- [108] Zimmerman G. and Kruer W. 1975 Numerical simulation of laser-initiated fusion *Comments Plasma Phys. Control. Fusion* **2** 51–60
- [109] Gomez M.R. *et al* 2017 Experimental study of current loss and plasma formation in the Z machine post-hole convolute *Phys. Rev. Accel. Beams* **20** 010401
- [110] Slutz S.A., Jennings C.A., Awe T.J., Shipley G.A., Hutsel B.T. and Lamppa D.C. 2017 Auto-magnetizing liners for magnetized inertial fusion *Phys. Plasmas* **24** 012704
- [111] Shipley G.A., Awe T.J., Hutsel B.T., Slutz S.A., Lamppa D.C., Greenly J.B. and Hutchinson T.M. 2018 Megagauss-level

- magnetic field production in cm-scale auto-magnetizing helical liners pulsed to 500 kA in 125 ns *Phys. Plasmas* **25** 052703
- [112] Shipley G.A., Awe T.J., Hutsel B.T., Greenly J.B., Jennings C.A. and Slutz S.A. 2019 Implosion of auto-magnetizing helical liners on the z facility *Phys. Plasmas* **26** 052705
- [113] Stygar W.A. *et al* 2015 Conceptual designs of two petawatt-class pulsed-power accelerators for high-energy-density-physics experiments *Phys. Rev. Spec. Top. Accel. Beams* **18** 110401
- [114] Slutz S.A. 2018 Scaling of magnetized inertial fusion with drive current rise-time *Phys. Plasmas* **25** 082707
- [115] Nora R. *et al* 2014 Theory of hydro-equivalent ignition for inertial fusion and its applications to omega and the national ignition facility *Phys. Plasmas* **21** 056316
- [116] Slutz S.A. 2021 private communication.
- [117] Nehl C.L., Umstatt R.J., Regan W.R., Hsu S.C. and McGrath P.B. 2019 Retrospective of the ARPA-E ALPHA fusion program *J. Fusion Energy* **38** 506
- [118] Zhang Y. *et al* 2019 Sustained neutron production from a sheared-flow stabilized z pinch *Phys. Rev. Lett.* **122** 135001
- [119] Slough J., Votroubek G. and Pihl C. 2011 Creation of a high-temperature plasma through merging and compression of supersonic field reversed configuration plasmoids *Nucl. Fusion* **51** 053008
- [120] Rahman H.U. *et al* 2019 Ar and Kr on deuterium gas-puff staged z-pinch implosions on a 1 mA driver: experiment and simulation *Phys. Plasmas* **26** 052706
- [121] Sinars D.B., Campbell E.M., Cuneo M.E., Jennings C.A., Peterson K.J. and Sefkow A.B. 2016 The role of magnetized liner inertial fusion as a pathway to fusion energy *J. Fusion Energy* **35** 78
- [122] Slutz S.A., Olson C.L. and Peterson P. 2003 Low mass recyclable transmission lines for Z-pinch driven inertial fusion *Phys. Plasmas* **10** 429
- [123] Grant Logan B. 1993 Inertial fusion reactors using Compact Fusion Advanced Rankine (CFARII) MHD conversion *Fusion Eng. Des.* **22** 151
- [124] Slutz S.A., Olson C.L., Rochau G.E., Derzon M.S., Peterson P., Degroot J., Jensen N. and Miller G. 2000 *Tech. Rep.* Albuquerque, NM Sandia National Laboratories